CHAPTER-3

Crystalline/crystalline interfaces in multilayer Au/Cu thin films

3.1 Introduction

Gold in its pure and alloyed form has been in use since time incognito for ornamental and decorative purposes [222]. Discovery of exciting properties at nano scales has given a fresh research impetus to this alloy system. Noble metals and alloys have emerged as a potential candidate in nanoelectronics, catalysis, bio-medical application, important component for targeted drug delivery etc. [100,223,224]. Their transport properties at the nanometer length scale, are influenced by the grain boundaries, defects, high surface to volume ratio. [50,225,226]. It is often believed that novel design of this alloy may result in reduction in transport losses, heat generation induced degradation of the interconnects as well as improvement in delay characteristics. All these in turn, will result in enhancement in life and energy saving characteristics of the devices [223,227]. In the field of catalysis, this alloy may revolutionize the current technologies so far as the cost of energy generation is concerned. Nanomaterials are also preferred in plasmonics and biomedicines [224,228]. It is well recognized that surface characteristics, atomic arrangements at the nanoscale and consequent changes in the electronic structure are of fundamental importance. Former two pertains to structural aspects. This is one of the prime objectives of this chapter as such aspects are relatively lesser understood in existing literature.

The equilibrium phase diagram of Au and Cu presents intriguing features (Figure 3.1) [100]. At higher temperature this binary system forms cubic solid solution as both Au and Cu satisfies the classical Hume-Rothery rule for solid solution formation and near equiatomic composition it exhibits a nearly congruent melting at (~910 ºC) with 44 at.% Cu. However, at a lower temperature below (~410 ºC), phase transformations of the FCC solid solution phase take place giving rise to many intermetallic phases e.g. CuAu, Cu_3Au, Au_3Cu, and CuAu II depending on composition.

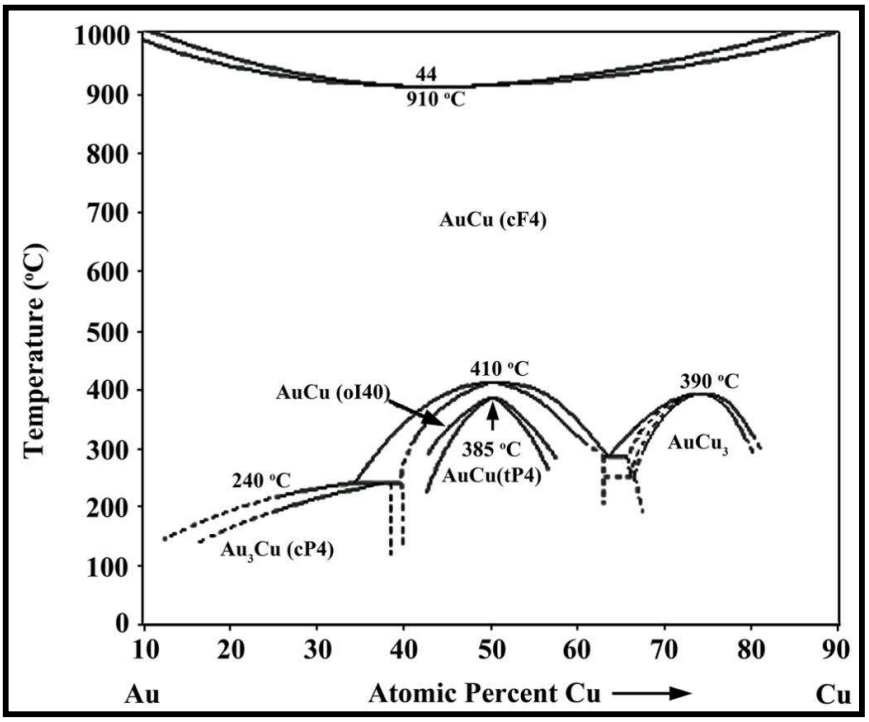

Figure 3.1: *Phase diagram of Au-Cu system showing the existence of equilibrium solid solution phase above 410°C along with intermetallics formation below this temperature over a wide composition range after Fig. 1 of [100].*

Even though considerable efforts have gone in the past in determining their equilibrium stability range and the nature of transformation [229], they have not been successful in completely delineating equilibrium phase fields in Au-Cu system. Consequently, many of the phase fields are marked as dotted line. In addition, many of these intermetallic phases undergo order-disorder transformation over a temperature range [230]. Investigations on this alloy system at nanoscale has augmented a new dimension to their phase transformation behavior. Reports have shown that the phase field boundaries undergo substantial changes at such length scales [115,231]. Additionally, in several studies it has been shown that many complex and long period superlattices are also formed in this alloy when it experiences metastable or non-equilibrium conditions during processing [112,113].

The difficulty in understanding many pertinent questions of phase transformation in this alloy is mainly attributable to the quite similar nature of the parent and product phases in terms of lattice parameter, atomic arrangements etc., which cannot be resolved through conventional techniques of X-ray diffraction and electron microscopy. Owing to such difficulties, the nature of heterophase interfaces formed between different structures has not been elucidated. Limited number of studies in this regard are available in literature especially at nanoscales [99,231,232]. It is important to understand and delineate issues of structural phase transformations that dictates the functional properties of the alloy system at nanoscale [233].

The current investigation was taken up to study the evolution of phases and nature of interfaces in multilayer thin films of gold and copper. Such thin film studies are important for their application in the area of nanoelectronics. In the present work, nanostructured multilayer thin films of Au and Cu were deposited onto polycrystalline Si substrate. The details of synthesis and tools utilized for structural characterization have been presented in chapter 2. Relevant experiment procedures for Au/Cu multilayers are given in the following section.

3.2 Experimental procedure

3.2.1 Thin film deposition

Au/Cu multilayer thin films were deposited onto polycrystalline Si substrate by thermal evaporation technique. Au and Cu were taken as starting materials for the deposition of multilayer thin films with each metal being > 99.95 % pure. Polycrystalline Si was taken as a substrate material in order to avoid the development of any kind of epitaxy during the deposition of the thin film onto the substrate. The substrate was cleaned by the standard process (level-I) (Section 2.2.1, Chapter-2). Prior to the deposition of the multilayer Au/Cu

thin films, it was planned to keep the thickness of each alternative individual layer of Au and Cu to be the same and the total number of layers up-to four. Restricting the number of layers up to four was intended to avoid the delamination of the multilayer thin films from the substrate. Following the aforementioned steps, the multilayers were deposited in the following sequence as poly Si/Cu/Au/Cu/Au, each individual layer of Au and Cu being ~40nm thick. Hereafter, such sample will be referred to as 40TAu. The Au/Cu multilayer thin film sample was vapor deposited using thermal evaporation technique under a vacuum of ~4 x 10^{-6} Torr. In the thermal evaporation process, the individual layers of Au and Cu were deposited in alteration, one after another onto the polycrystalline Si substrate that was kept at room temperature. The deposition rate was varied in the range ~ 0.001- 2 Å/s depending on the current applied, whereas the current for evaporating Au and Cu was controlled separately up to ~40 mA. The thickness of layer being deposited was monitored with the help of thickness monitor display. The position of the substrate pieces within the evaporation chamber with respect to the source position was varied from perpendicular direction to some inclined position (cf. figure 2.1).

3.2.2 Grazing incidence X-ray diffraction (GIXRD)

GIXRD has been done following the in-plane diffraction condition using high resolution XRD (Rigaku SmartLab operating at 45kV and 200 mA) using X-rays with λ ~1.542Å. Cu-K_α target was used. Sample was scanned from 10° to 90° angles at several incidence angles ranging from 0.1° to 3° but the best intensities of peaks were found at 0.45°.

3.2.3 TEM cross-section specimen preparation

Electron transparent cross-section samples were prepared from the Au/Cu multilayer thin films on polycrystalline Si substrates by conventional sample preparation technique. Details of the sample preparation have been given in Section 2.3.1 (Chapter 2). Afterwards,

these cross-section thin film specimens were used for transmission electron microscopy (TEM), high resolution (HRTEM) phase contrast imaging and STEM-EDS mapping. The structural investigation of the multilayer film itself and of the interfaces had been done using Tecnai G^2 T20 (C_s= 1.2 mm) TEM operated at 200 kV.

Table 3.1: *Structural parameters used in multislice simulation.*

S. No.	Struc.	Lattice Parameter (nm)	Space Group (No.)	Wyckoff Positions (site)	Coordinates	Occ.
1	oP8	a= 0.892 b= 0.452 c= 0.283	Pbam (55)	4h (Cu1) 4h (Cu2) 4h (Cu3) 4h (Cu4)	0.479, 0.960, 0.5 0.155, 0.758, 0.50 0.655, 0.46, 0.5 0.979, 0.258, 0.5	1 1 1 1
				4g (Au1) 4g (Au2) 4g (Au3) 4g (Au4)	0,0,0 0.634,0.718,0 0.134,0.5,0 0.5,0.218,0	1 1 1 1
2	oI40	a= 0.367 b= 0.395 c= 3.97	Imma (74)	4e (Cu1) 4e (Cu2) 4e (Cu3) 4e (Cu4) 4e (Cu5)	0, 0.25, 0.526 0, 0.25, 0.424 0, 0.25, 0.626 0, 0.25, 0.323 0, 0.25, 0.727	1 1 1 1 1
				4e (Au1) 4e (Au2) 4e (Au3) 4e (Au4) 4e (Au5)	0, 0.25, 0.025 0, 0.25, 0.925 0, 0.25, 0.125 0, 0.25, 0.826 0, 0.25, 0.224	1 1 1 1 1
3	tP4	a=b= 0.396 c= 0.367	P4/mmm (123)	2e (Cu1)	0, 0.5, 0.5	1
				1a (Au1)	0,0,0	1
				1c (Au2)	0.5,0.5,0	1
4	cP4	a=b=c= 0.398	$Pm\bar{3}m$ (221)	1a (Cu1)	0,0,0	1
				3c (Au1)	0,0.5,0.5	1

3.2.4 Simulation of grazing incidence x-ray patterns and high resolution images

The information obtained from GIXRD experiment is not enough to uniquely identify various phases present in the Au/Cu multilayer thin films as they have similar d-spacings. The XRD simulations of all the phases that are available in literature at equiatomic and at

non-equiatomic compositions have been done with a reference to their corresponding JCPDS files. Six simulated patterns have been generated for AuCu phases with cF4, oP8, tP4, oI40 and cP4 structures. Later on, each of these simulated patterns has been compared with the experimental one to arrive at a conclusion pertaining to the formation of phase(s). The quantification and simulation of TEM micrographs of oP8 (AuCu), oI40 (AuCu), tP4 (AuCu) and cP4 (Au_3Cu) phases, present at the interfaces in Au/Cu multilayer thin films, have been done using Gatan Digital Micrograph software and Java based JEMS simulation software [158]. The HRTEM image along a particular zone axis is simulated by the 'multi-slice' method. Diffraction simulation is carried out under multiple beam dynamical condition and the crystal thickness is considered to be ~12 nm for AuCu (oP8), ~22 nm for AuCu (oI40), ~7 nm for (AuCu) tP4 and ~11 nm for Au_3Cu (cP4). Crystallographic details of the phases, which have been used for simulations are given in table 3.1.

3.3 Results

3.3.1 GIXRD and simulation

Figure 3.2 shows the GIXRD of the 40TAu thin film multilayer sample. Simulated polycrystalline diffraction patterns of several possible intermetallic phases in Au-Cu system are also included in this figure as multiple display. The average strain value is ~ 0.025 and the crystallite size varies in the range of ~4-30 nm. The details of crystallite size and the value of strain is given in Table 3.2. The experimental GIXRD pattern as shown in figure 3.2 contains peaks having close match with the solid solution of AuCu (cF4) phase. However, profile fittings of various peaks reveals shouldering and splitting, indicating the presence of a mixture of phases in the sample.

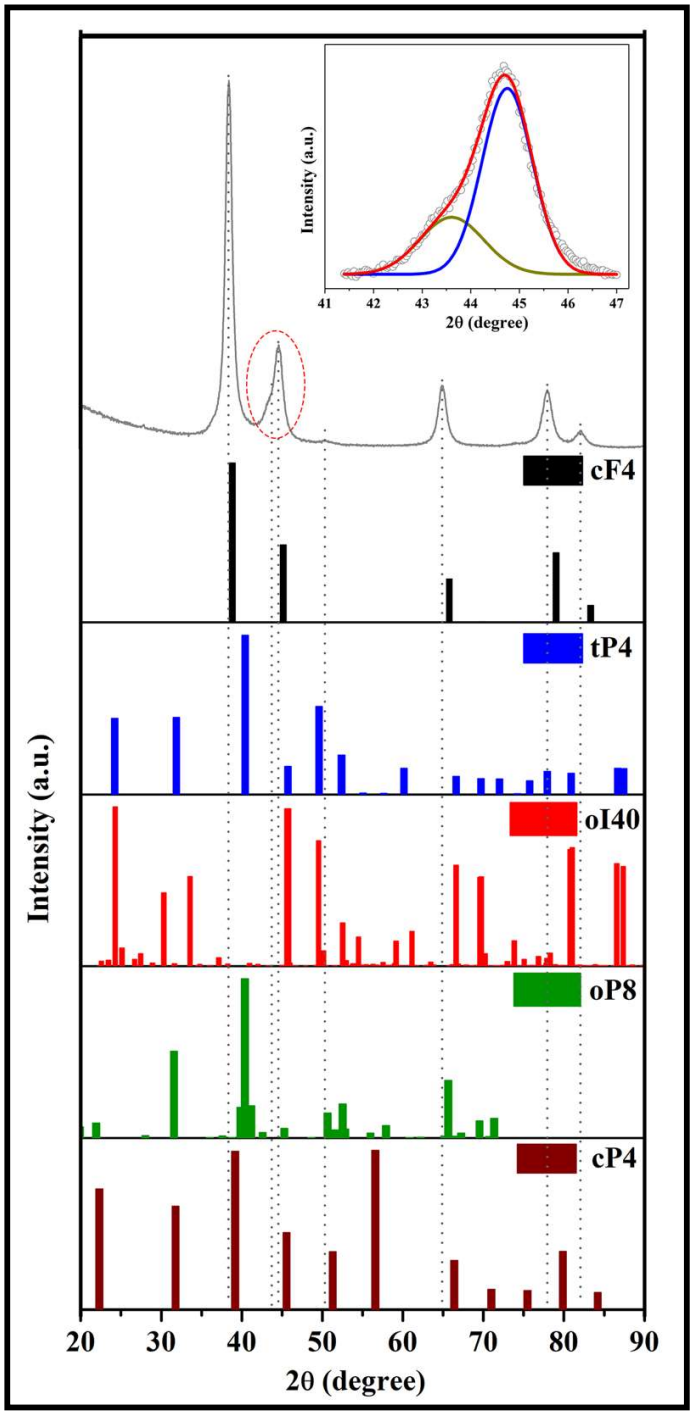

Figure 3.2: *Experimental GIXRD pattern of multilayer Au/Cu thin film (Top in the multiple display). Enlarged version of the encircled region is given at the inset. Simulated patterns of possible Au-Cu phases with cF4, tP4, oI40, oP8 and cP4 structures are placed underneath for comparison.*

Table 3.2: *Calculated crystallize size and average strain from the Au/Cu thin film.*

S. No.	θ (degree)	β (degree)	cosθ (degree)	~ d (nm)	βcosθ	sinθ (degree)	Average Strain
1	19.2	0.3	54.1	30	0.2	18.8	~0.025
2	21.7	2.3	53.2	4	2.2	21.2	
3	22.3	0.3	52.9	25	0.3	21.7	
4	32.4	0.5	48.3	18	0.4	30.7	
5	38.9	0.7	44.5	14	0.6	36.0	
6	41.0	1.0	43.1	11	0.7	37.6	

For example, the second peak having a spread of 2θ between 42.58° to 46.18°, has the signature of peak splitting/shouldering. This peak splitting (encircled) was deconvoluted and the same has been shown in the inset of figure 3.2. This deconvolution result showed that the second peak consists of two peaks. One shown in green, appeared at 2θ = 43.5° and the other in blue at 44.67°.

Simulated XRD patterns were generated for the phases formed at equiatomic and non-equiatomic compositions in Au-Cu phase diagram in order to assess their presence in the film. The simulated XRD patterns for cF4 (AuCu), tP4 (AuCu), oP8 (AuCu), oI40 (AuCu) and cP4 (Au_3Cu) phases also match closely with the experimental pattern with some minor shift. cF4 (AuCu) is a disordered solid solution phase and oP8 (AuCu), oI40 (AuCu), tP4 (AuCu) are ordered phases. Another intermetallic phase refers to cP4 (Au_3Cu) is also ordered phase. When the simulated XRD pattern of disordered cF4 (AuCu) phase was compared with the experimental GIXRD pattern, it was observed that all the peaks represented by dotted line) in the experimental pattern were shifted towards the left side with respect to simulated cF4 peaks. However, the simulated peak positions are within the limit of broadening of the experimental pattern.

Table 3.3a: *Comparison of experimentally observed diffraction maxima along with their intensities and d-spacings with the simulated diffraction maxima and intensities for AuCu cF4, and tP4 structures.*

Experimental					Simulated			
S. No.	2θ (deg.) range	2θ at max. intensity	d (nm)	Peak intensity (a.u)	AuCu (cF4)			
					2θ	d-spacing (nm)	Miller indices	Intensity (a.u.)
1	37.6 – 39.8	38.5	0.233	999	38.8	0.231	(111)	999
2	42.6 – 46.2	43.5, 44.7	0.208,0.203	128, 287	45.2	0.201	(200)	485
3	49.2-51.6	50.4	0.179	26	-	-	-	-
4	63.1-66.7	64.9	0.143	176	65.8	0.141	(220)	282
5	75.8-80.0	78.0	0.122	165	79.1	0.121	(311)	437
6	80.9-83.5	82.1	0.117	55	83.4	0.116	(222)	106
					AuCu (tP4)			
1	37.6 - 39.8	38.5	0.233	999	40.5	0.222	(111)	999
2	42.6 – 46.2	43.5, 44.7	0.208,0.203	128, 287	45.7	0.198	(200)	176
3	49.2-51.6	50.4	0.179	26	49.6	0.183	(002)	553
4	63.1-66.7	64.9	0.143	176	66.7	0.140	(220)	113
5	75.8-80.0	78.0	0.122	165	77.9	0.122	(003)	144
6	80.9-83.5	82.1	0.117	55	80.9	0.118	(311)	132

This observation led to the inference that there is an increase in the interplanar spacing of all the diffracting planes in solid solution (cF4) phase, which also resulted in increased lattice parameter in solid solution (cF4) phase. The 2θ values for comparison between experimental and simulated peaks are given in table 3.3a and 3.3b.

Table 3.3 b: *Comparison of experimentally observed diffraction maxima along with their intensities and d-spacings with the simulated diffraction maxima and intensities for AuCu oI40, oP8, and cP4 structures.*

Experimental					Simulated			
S. No.	2θ (deg.) range	2θ at max. intensity	d (nm)	Peak intensity (a.u)	2θ	d-spacing (nm)	Miller indices	Intensity (a.u.)
					AuCu (oI40)			
1	37.6 – 39.8	38.5	0.233	999	38.3	0.234	(1 0 13)	13
2	42.6 – 46.2	43.5, 44.6	0.208,0.203	128, 287	43.2, 45.0	0.208, 0.201	(1 1 12), (0 1 17)	1-5
3	49.2-51.6	50.4	0.179	26	50.2	0.181	(1 0 19)	95
4	63.1-66.7	64.9	0.143	176	63.9	0.145	(1 2 15)	7
5	75.8-80.0	78.0	0.122	165	77.9	0.122	(3 0 1)	48
6	80.9-83.5	82.1	0.117	55	82.0	0.117	(2 0 26)	6
					AuCu (oP8)			
1	37.6 – 39.8	38.5	0.233	999	38.7	0.232	(111)	2
2	42.6 – 46.2	43.5, 44.7	0.208,0.203	128, 287	42.6, 45.3	0.212, 0.20	(211), (410)	33-58
3	49.2-51.6	50.4	0.179	26	50.7	0.180	(320)	156
4	63.1-66.7	64.9	0.143	176	65.2	0.143	(511)	9
					AuCu (cP4)			
1	37.6 – 39.8	38.5	0.233	999	39.2	0.229	(111)	996
2	42.6 – 46.2	43.5, 44.7	0.208,0.203	128, 287	45.5	0.199	(200)	485
3	49.2-51.6	50.4	0.179	26	51.3	0.177	(210)	363
4	63.1-66.7	64.9	0.143	176	66.4	0.140	(220)	308
5	75.8-80.0	78.0	0.122	165	79.8	0.120	(311)	365

As the experimental diffraction peaks represent a combination of different phases with the highest intensity points belonging to the cF4 phase. Based on this, the lattice parameter and the composition of the solid solution phase is calculated to be a = 0.403 nm and Au = 88 at%. To detect the presence of other intermetallic phases, the simulated XRD pattern of tP4 phase was also compared with the experimental pattern. A left shift was observed in the experimental peaks with respect to 111, 200 and 220 reflections in simulated tP4 phase (cf. table 3.3a). A right shift was observed in 002 and 311 planes whereas the 003 plane was exactly matched. This overall non-uniform shift in the diffracting peaks of experimentally obtained pattern may be attributed to the presence of strain, defects and local non-stoichiometry. Comparison of the simulated diffraction pattern of oI40 phase brings about excellent match with the experimental one except a few peaks are missing. This may be attributed to the low volume fraction of oI40 phase due to which the intensities of many peaks are below the detectable limit. Additionally, there may be some orientation relationship with the solid solution phase, which has led to absence of some peaks.

To delineate the presence of other intermetallic phases, the simulated oP8 pattern was compared with that of the experimental one. In this observation most of the planes such as 111, 320 and 511 in simulated oP8 phase had exactly matched with experimental peaks whereas 211 and 410 planes showed very little shift from experimentally observed peaks (cf. table 3.3b). This analysis confirmed the presence of oP8 phase in thin film. However, the cP4 phase exists in two forms, one is Au_3Cu and another is Cu_3Au. In the present study no significant match was found even close to simulated cP4 (Cu_3Au) phase, hence the possibility of existence of this phase is ruled out. When simulated cP4 (Au_3Cu) phase was compared with GIXRD pattern, again the left shift was observed in all the experimentally observed peaks.

The shift was found to be more in the last three peaks of experimental pattern with respect to its first three peaks. Moreover, the planes observed in the ordered phases such as tP4, oP8, oI40 and cP4 with 2θ less than 35° were not clearly discerned in the experimental pattern. This may remain unnoticed due to their low integrated intensities added with the low phase fractions compared to the disordered solid solution phase. Any attempt to quantify the phase fraction may largely be in error and has not been attempted. When the broadening range in each experimental peak was taken into consideration, it was observed that all the peaks in each of the simulated patterns were falling under the observed broadening range. This indicates that the presence of all these ordered phases along with the solid solution phase ultimately leads to the deviations in 2θ values of experimental pattern from their respective standard equiatomic as well as non-equiatomic phases available in literature [179,229].

3.3.2 Diffraction contrast imaging, morphology and chemistry

Cross-section transmission electron microscope (XTEM) bright field image of 40TAu is shown in figure 3.3a. In this XTEM image, the bottom part with grey contrast is the polycrystalline Si substrate. First layer deposited is Cu on the Si substrate. Above the Cu layer, Au layer was deposited. This deposition was continued in alternate fashion up to four layers, pertaining to which, two interfaces between Au and Cu were created within the Au/Cu multilayer thin film. The Cu layers in the multilayer Au/Cu thin films are not showing strong crystallographic contrast arising out of grain boundaries, defects and strain fields, while the Au layers are visibly showing strong crystallographic contrast. It had been observed from the BF image that the film is not very much uniform along the length. The average thickness of the film has been observed to be ~65 nm with a variation in thickness of ~8 nm.

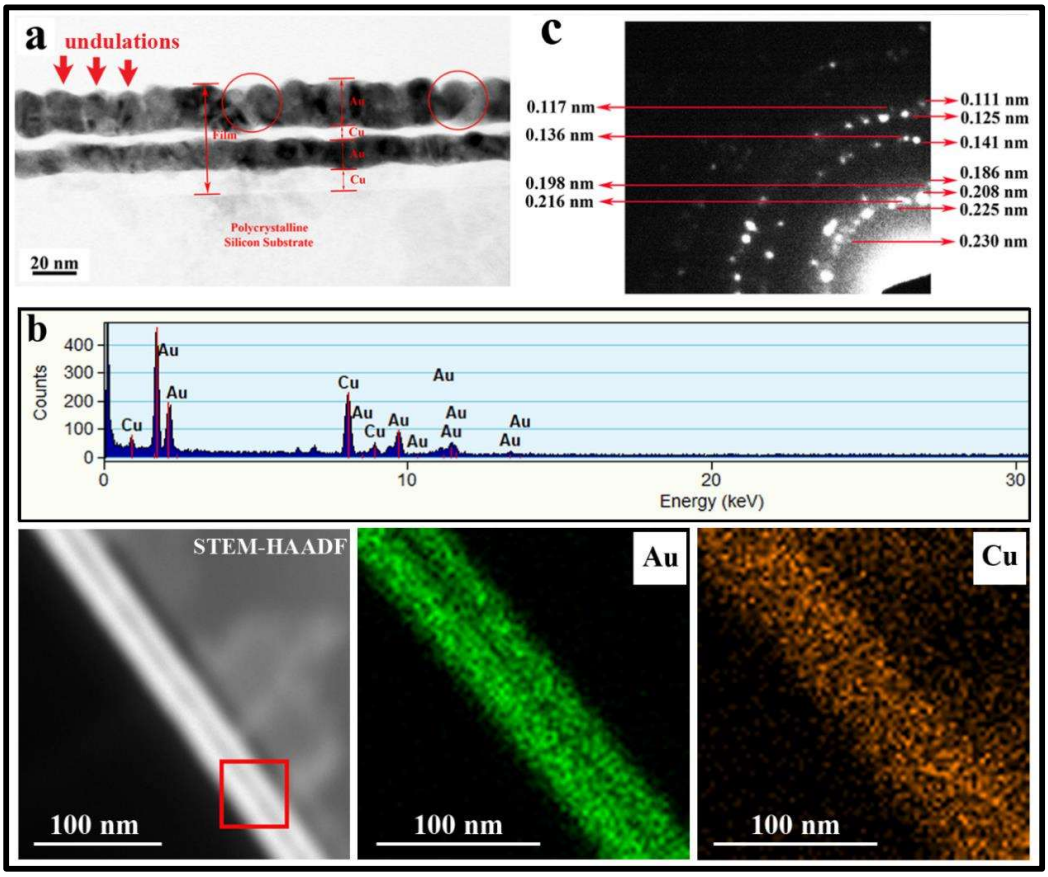

Figure 3.3: a) *TEM bright field image showing the cross-section view of Au/Cu multilayers along with the polycrystalline Si substrate. Individual Au and Cu layers along with the polycrystalline Si substrate has been marked* ***b)*** *X-ray energy dispersive spectrum (XEDS) and spectral map from the multilayer thin film. Extensive interdiffusion is observed across the interface of the multilayer.* ***c)*** *corresponding selected area electron diffraction pattern obtained from the Au/Cu multilayers only. Experimentally obtained d-spacings have been marked in the diffraction pattern.*

The interface between Si and Cu appears quite sharp. However, a discontinuous weak contrast could be seen along the sharp Cu/Si interface. This contrast indicates that some reaction might have taken place at the Cu-Si interface, the depth of which is dependent on the kinetic energy of impinging Cu atoms on Si substrate. It can be said that more kinetic energy leads to a deeper penetration into the substrate and higher thickness of the reaction layer. Variation in contrast could be seen within the individual layers of Au and Cu also.

The variation in contrast in the Au layer is due to the difference in orientations of the individual diffracting crystals present in it. The undulations could also be seen at the interfaces of Cu /Au thin films (marked by arrows in figure 3.3a). The cross-section morphology of multilayer Au/Cu thin films exhibited columnar/cupola like shape, which consists of convex curvature in the middle of the columns as well as cusp like minima at the column walls. This is often termed as the waviness of the multilayers [41]. This waviness of the interface has gradually increased with the distance from the substrate i.e. the amplitude of the convex curvature in the multilayer thin film is less in the initial interface near the substrate and it is gradually increasing towards the top layer of the film. These vapor-deposited thin films are quite rough in nature with periodic interruptions along the column boundaries.

The columnar structure in Au layers along with the wavy surface and interfaces are not seen in Cu layers. The growth direction of the columns has been found to be perpendicular to the film substrate in most of the places except where the incidence of vapor was oblique to the substrate (encircled). Composition fluctuation at the inter-columnar space may be expected. The differences in the interatomic forces across the columns resulted in the variation of inter-columnar separation distance, which led to the generation of non-uniform stress inside the thin films [234]. The partial coverage of inter-columnar boundaries with low density areas encircled in figure 3.3a enhances short-circuit diffusion paths in a direction perpendicular to the film plane and is considered to be detrimental in diffusion based applications [44,235]. The crystallites present in the Au layer have been carefully observed. It is found that the crystallites perpendicular to the film surface/interface are almost similar in size to the film thickness and those inclined are little larger than the film thickness. Variation in crystallite size may be associated with the film thickness.

Furthermore, the diameter of the columns as measured for both the top and the middle Au layers are found to be dependent on the thickness of the Au layer. The average diameter and thickness of the columns in the top Au layer are ~12 nm and ~25 nm respectively whereas in the middle Au layer the average diameter and thickness were noticed to be ~9 nm and ~12 nm respectively.

The x-ray energy dispersive spectrum (XEDS) and the spectral map from the multilayer is given in figure 3.3b. It is observed from the spectrum that only Au and Cu are present in the multilayer. And the spectral map indicates that the individual layers are predominantly Au and Cu. However, extensive inter-diffusion of Au and Cu has taken place across the interface. The amorphization of the Cu layer should not be considered as an amorphization of a pure element. It is mostly the sluggish crystallization kinetics of the extremely thin Cu rich layer that leads to amorphization. It will be discussed subsequently.

3.3.3 Selected area diffraction (SAD)

Selected area diffraction (SAD) pattern as obtained from the multilayers in 40TAu specimen is displayed in figure 3.3c. The diffraction pattern shows some discontinuous spotty rings embedded in diffused hallo type contrast. These discontinuous spotty rings represent the polycrystalline nature of the multilayer Au/Cu thin films with the presence of a few nanometer sized crystals. In addition, the diffused halo in the background confirms the presence of amorphous regions in the thin film. Each broad ring in the SAD consists of two or more very closely spaced rings. As mentioned in the preceding section, this is the consequence of very close values of d-spacings present in the ordered as well as disordered phases present in Au-Cu system. The observed values of d-spacings have been compared with those of reported values for ordered and disordered phases in Au-Cu system and it is represented in table 3.4.

In table 3.4, it is shown that the reported values of d-spacing in ordered phases like oP8 (AuCu), oI40 (AuCu), tP4 (AuCu), cP4 (Au_3Cu) and disordered phase cF4 (AuCu) are very close to one another and in agreement with the experimental observation. With the analysis of this diffraction pattern, it can be said that the Au/Cu multilayer thin film is composed of solid solution (cF4) phase along with the intermetallic phases of Au and Cu. This qualitative assertion conforms to those mentioned in section 3.3.1.

3.3.4 High-resolution phase contrast imaging

Cross-section phase contrast TEM image of Au/Cu multilayer thin film at a relatively higher magnification is shown in figure 3.4a. In this image, muzzy contrast could be observed in Cu layers (white color). This muzzy contrast confirmed that the Cu layers did not crystallize and remained amorphous in the thin films. Au layers appeared to be crystalline in nature. The presence of moiré patterns (indicated by yellow arrows) within the Au layers confirms the polycrystalline nature of these layers. These moiré patterns further confirm the juxtaposition of two crystalline Au islands with some specific crystalline relationship [141]. However, presence of strain at the interface is quite likely. This overall analysis suggested that the Au was able to crystallize whereas Cu could not. Such a structural difference in Au and Cu layers is attributed to the slower kinetics of crystallization of Cu compared to that of Au [146,159]. Contrasts indicated by white arrows, mostly in the Au layer, are strain fields, which are generated due to non-equilibrium processing conditions during deposition (cf. Figure 3.4a). In this process, the Au crystals did not get sufficient time to relax strain. Features indicated by dotted yellow curved lines are the diffraction contrast features arising at the grain boundaries or inter-columnar boundaries[106]. Such boundaries are not very clearly defined. Undulations at the Au/Cu interfaces could be observed. Undulation and the presence of localized differential contrast

(marked by red arrow) at the interface may be indicative of atomic mixing at the interfaces [236,237]. This requires further investigation, which is addressed in the section 3.4.1.

Table 3. 4: *Comparison of the experimentally observed d-spacings from the SAD pattern as shown in figure 3c with the reported d-spacings of the ordered and disordered phases present in AuCu system.*

Observed d-spacing (nm)	**Reported d-spacing (nm) AuCu (cF4)**	**Reported d-spacing (nm) AuCu (tP4)**	**Reported d-spacing (nm) AuCu (oI40)**	**Reported d-spacing (nm) AuCu (oP8)**	**Reported d-spacing (nm) AuCu (cP4)**
0.230	0.231 (111)		0.234 (10,13)	0.232 (111)	
0.225		0.222 (111)	0.222 (11,10)	0.223 (400)	0.229 (111)
0.216			0.214 (10,15)	0.219 (120)	
0.208	0.201 (200)		0.208 (11,12)	0.200 (410)	
0.197		0.198 (200)	0.197 (020)		0.199 (200)
0.186		0.183 (002)	0.183 (200)	0.187 (311)	
0.141	0.141 (220)	0.140 (220)	0.141 (21,15)	0.141 (610)	0.140 (220)
0.136		0.134 (202)	0.136 (10,27)	0.135 (202)	0.132 (300)
0.125	0.121 (311)	0.122 (003)	0.125 (21,21)		0.125 (310)
0.117	0.116 (222)	0.118 (311)	0.117 (20,26)		0.114 (222)
0.111		0.111 (222)	0.111 (22,20)		0.110 (320)

3.3.4.1 Cu/Si interface and defects

High-resolution image of the Cu and Si interface is shown in figure 3.4(b-c). In figure 3.4b, the Cu layer is recognized by its muzzy bright contrast whereas the polycrystalline Au layer and Si substrate are identified as a dark contrast region on either side of the Cu layer. The region outlined by the dotted curve appeared amorphous as it is muzzy in appearance. However, its contrast is little weaker compared to amorphous Cu contrast, which may be

correlated with the difference in chemistry at the Cu/Si interface. The right side region adjacent to it is covered with lattice fringes representing interplanar spacing of ~0.301 nm. The value of this interplanar spacing matches with $(1\,\bar{1}\,1)$ plane of Si. It has diamond cubic structure with 2 atoms per lattice point having Pearson symbol cF8. The lattice parameters are a = b = c = 0.521 nm and $\alpha = \beta = \gamma = 90°$. It falls in the space group $Fd\bar{3}m$ (space group no. 227) with allowed center of symmetry. The orientation of this particular grain in Si substrate was found to be along $[\bar{1}\ 1\ 2]$ zone axis, which was confirmed by its SAD pattern displayed in the inset of figure 3.4b. Figure 3.4c is the high-resolution phase contrast image obtained from the region little inside the Si substrate. In this image also, the clearly appearing lattice fringes were from $\{1\,\bar{1}\,1\}$ planes of Si. A dotted outline region (~ 8 nm) inside the substrate represents the uneven appearance of lattice fringes and beyond this region inside the substrate they started disappearing. It is important to note that the blurring of these fringes along with white contrast is observed in the bottom right corner of this image. Such a white contrast has resulted due to the defect cascades in this region [238]. The FFTs obtained from the dotted square regions within this area can be seen in the insets of figure 3.4c. When these FFTs were analyzed separately, a considerable difference of ~0.01 nm was obtained within the spacing of the $(1\,\bar{1}\,1)$ and (220) planes of Si substrate. This significant difference of ~0.01 nm due to defect cascade can clearly be observed in (inverse) IFFTs as given in figure 3.4e and figure 3.4f (defect cascade region) respectively. Moreover, a distortion in the appearance of lattice fringes corresponding to $(1\,\bar{1}\,1)$ and (2 2 0) planes is also discerned in figure 3.4f.

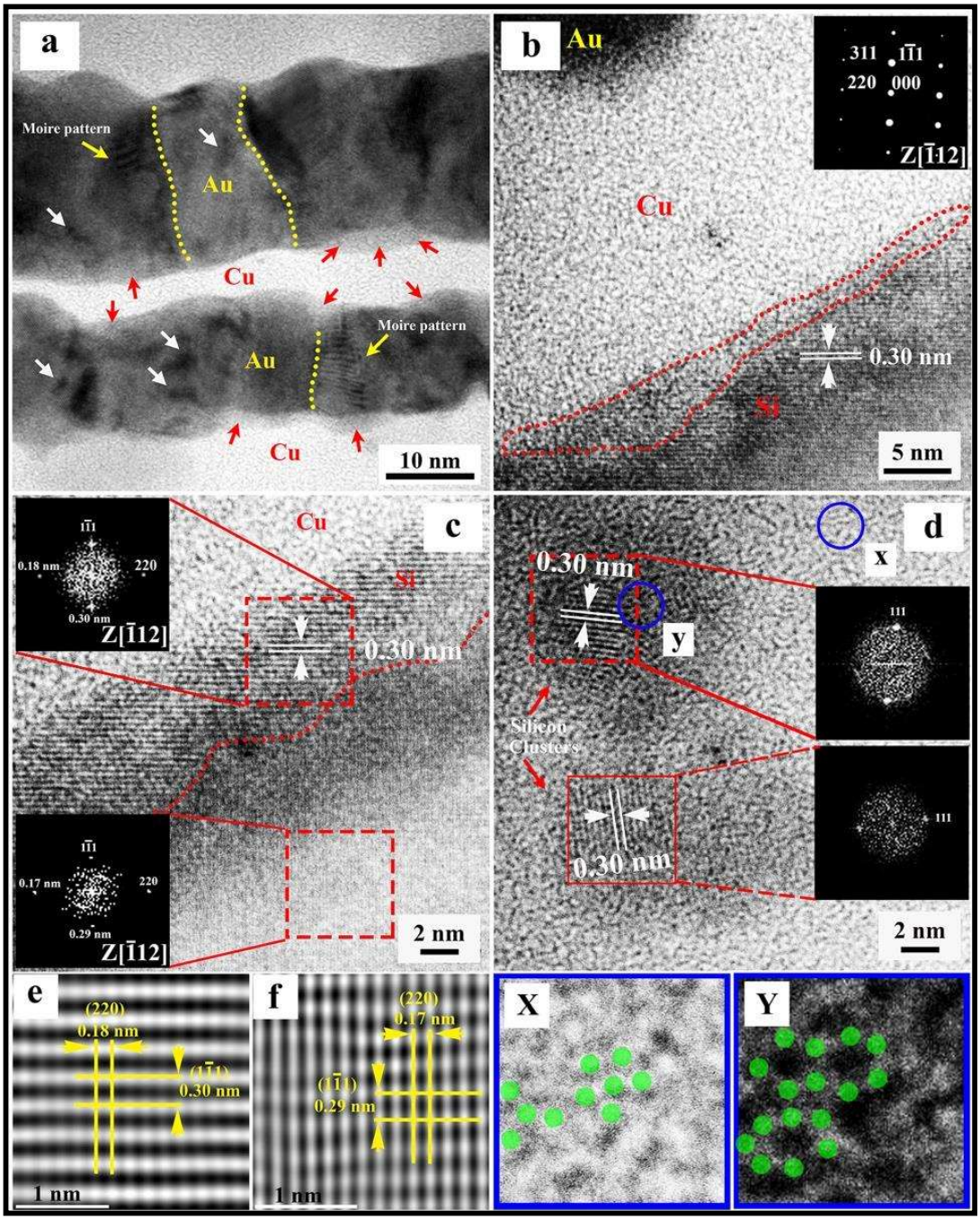

Figure 3.4: a) *Cross-section high magnification diffraction contrast image of Au/Cu multilayers representing the individual amorphous Cu layer and Au crystalline layer. Interface reactions and morphology, moire patterns and inter-columnar boundaries have also been indicated by arrows and dotted curves respectively. White arrows represent remnant strains during non-equilibrium solidification* ***b)*** *cross-section high resolution*

phase contrast image of the film-substrate interface. Dotted curve indicates the reaction product of Cu-Si interface. Inset shows the SAD of Si grain oriented along $[\bar{1}\,1\,2]$ *zone axis.* ***c)*** *cross-section high resolution phase contrast image of amorphous Cu/Si interface. Wavy dotted curve within the substrate demarcates the boundary beyond which lattice fringes disappear. Two different contrast regions marked by dotted squares named as* ***'e'*** *and* ***'f'*** *along with their corresponding FFTs (represented at the insets) and inverse FFTs as displayed in figure 3.4e and figure 3.4f respectively.* ***d)*** *High-resolution phase contrast image obtained from the region few nm inside the surface of the substrate showing Si clusters as indicated by arrows those are surrounded by amorphous Si. Corresponding FFTs obtained from the Si clusters are shown in the insets. Regions 'x' and 'y' within the amorphous Si as indicated by solid circles are cropped and shown separately in figure 3.4X and figure 3.4Y respectively. Amorphous Si features like floating bonds and dangling bonds are displayed in figure 3.4X whereas five, six and seven membered rings are represented in figure 3.4Y with colored dots.*

Figure 3.4d depicts a completely amorphous Si along with some short range ordered clusters inside ~10 nm from the surface of a substrate. The lattice fringe spacing from these clusters were measured to be ~0.301 nm and matched with the family of {1 1 1} planes of Si. The same is substantiated with their corresponding FFTs shown in the insets. Therefore, it is clear that a few crystalline Si clusters are present within the region of disordered amorphous Si. The contrast of the crystalline as well as amorphous domains within the same cluster looks distinct from the completely amorphous Si because of their orientation. This crystalline to amorphous phase transformation in Si might have occurred due to Ar-ion implantation during ion-milling of the specimen. These irradiating ions made the crystalline Si unstable by creating a planar front on its either sides with distinct interfaces separating its amorphous and crystalline phases. This amorphous layer thickened with continued implantation leaving behind a few short range ordered clusters. The magnified version of region 'x' and region 'y' are given in figures 3.4X and 3.4Y respectively. The

contrast in these regions is not completely muzzy. However, systematic appearance of bright and dark dots may represent dangling bonds, floating bonds and finite member atomic rings [239].

3.3.4.2 Au/Cu interfaces and defects

High-resolution phase contrast images obtained from various regions within the multilayer Au/Cu thin films are shown in figure 3.5. In figure 3.5a, a few regions were observed to be oriented along certain zone axes, which are encircled with dotted circle and were found to be different in appearance, and therefore, are marked as 'A' and 'B' regions. The faceting could clearly be observed at the periphery of region 'A' as represented with solid outline. However, those were not very clear around region 'B'. The regions 'A' and 'B' can be identified as oI40 (AuCu) and oP8 (AuCu) phase respectively. The details of the phase identification have been discussed later. The facet planes associated with the region 'A' are (1 1, 10) and (1 0 $\bar{5}$). The corresponding d-spacings are ~0.220 nm and ~0.337 nm respectively (Figure 3.6a). These facet planes are representative of the interface between the solid solution phase of Au-Cu and the intermetallic phase nucleated in it. They provide critical information about the nature of transformation, the interface and the strain associated with it. This matter would be discussed subsequently. However, the twin boundary could also be observed, which is represented by dotted line (Figure 3.5a). Such a twin boundary disappeared beyond a few nanometers. The region represented by a solid yellow rectangle displays the region where the twin boundary is disappeared followed by some distortion and moiré formation. Moreover, the same kinds of oriented regions within the columns are also observed in different portions of Au/Cu multilayer thin films marked as 'C' and 'D' regions (encircled with dotted circle) in figure 3.5b.

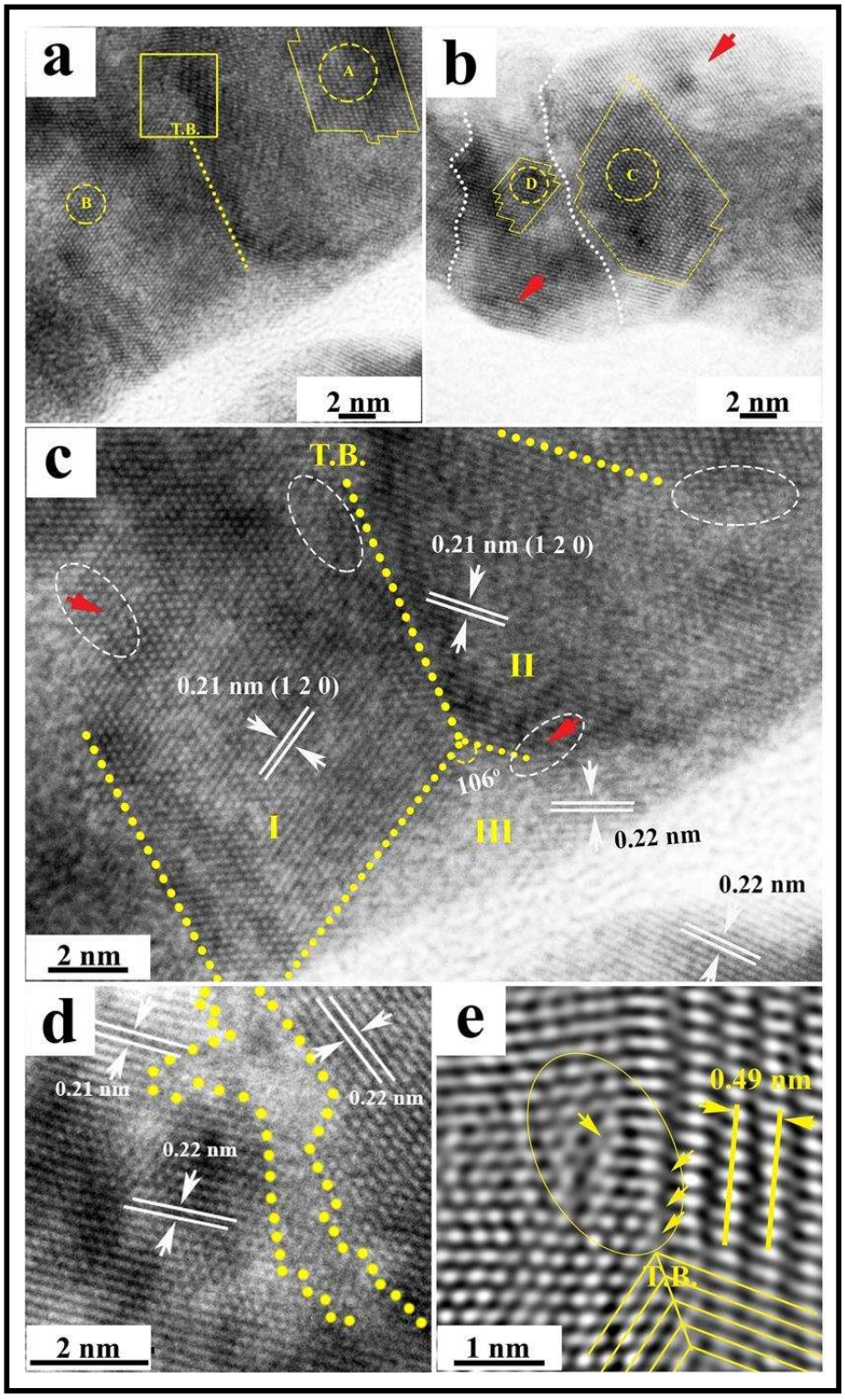

Figure 3.5: *High-resolution phase-contrast images showing cross-section views of various regions in Au/Cu multilayered thin film* ***a)*** *A crystalline Au layer showing nano-twin*

boundary along with some ordered regions marked as 'A' and 'B'. Interface formed between differently ordered regions consisting of kinks and ledges along the periphery of 'A' as shown by solid color lines. ***b)*** *Representation of inter-columnar boundaries as white dotted curves within the crystalline layer of thin film. Ordered regions marked as 'C' and 'D' display differently ordered interfaces consisting of kinks and ledges as highlighted by solid color lines. Colored arrows show the defects within a grain of Au* ***c)*** *high magnification HRTEM image of the twinned region displaying three differently oriented islands marked as I, II and III.* ***d)*** *Representation of the disordered region formed between differently oriented islands.* ***e)*** *Region displaying defects just above the twin boundary as marked by solid square in figure 3.5a.*

Peripheries of these 'C' and 'D' regions also consist of ledges and kinks (represented by outer line). The enlarged version of the faceted regions is given in figures 3.6a and 3.6b. In figure 3.6b, the faceted regions could be identified as oI40 (AuCu) (region C) and tP4 (AuCu) (region D). The facet planes for the tP4 structure could be identified as (1 1 1) and the d-spacing is ~0.219 nm. It is worth-noting that the facet planes are almost atomically aligned with the parent cubic solid solution phase. The consequence of this will be quantitatively discussed in the section 3.4.3 once the images are understood better by simulation.

It is important to note that, only the phase contrast across the facets changes, so understanding the phase contrast images through simulation is critical to comprehending the nature of the interface, mechanism of the transformation etc. The inter-columnar boundaries (displayed in dotted curves) could also be observed along with the disordered bright contrast all-throughout these boundaries. In figures 3.5a and 3.5b, the encircled regions marked as 'A' and 'C' respectively, are identified as an ordered oI40 (AuCu) phase. However, the encircled regions 'B' and 'D' shown in figures 3.5a and 3.5b are found to be ordered oP8 (AuCu) and tP4 (AuCu) phases respectively. The analyzed and processed

phase contrast images along with their corresponding FFTs (inset) from all of these ordered phases seen in Au/Cu multilayer thin films are displayed in figure 3.7. In figure 3.7a, ordered oP8 (AuCu) phase is viewed along [0 1 0] zone axis whereas the reflecting planes parallel to this zone axis are (4 0 0) and (2 0 1) at an angle of 58°. The d-spacing values for (4 0 0) and (2 0 1) planes are ~0.220 nm and ~0.230 nm respectively. Ordered oI40 (AuCu) phase has been shown separately in the figure 3.7b. In this high resolution image the structure of oI40 phase was looked along $[\bar{5},\ 15\ \bar{1}]$ zone axis whereas the reflecting planes parallel to this zone axis were found to be $(1\ 0\ \bar{5})$ and (1 1, 10) at an angle of 72°. The d-spacing values for $(1\ 0\ \bar{5})$ and (1 1, 10) planes are ~0.330 nm and ~0.220 nm respectively. The oI40 is considered to be a superstructure in literature with the presence of anti-phase boundaries in it [112]. However, anti-phase boundaries are not visible in the present case. The reason being that translation vector for the anti-phase boundaries in oI40 is ½ {1 0 1} family of directions. There could be various possible directions through which this anti-phase boundary would develop δ-fringe contrast [240,241]. However, that would require setting up a proper two-beam condition and diffraction contrast imaging. As the crystal size is pretty small and the images are taken in phase contrast mode, the anti-phase boundary remains invisible. In phase contrast image mode, anti-phase boundary could only be seen and analyzed when the crystal is imaged along [1 0 0] or [0 1 0]. In this case the crystal orientation being different from these directions, the anti-phase boundary remains invisible. In addition to this, figure 3.7c represents phase contrast image of ordered tP4 (AuCu) phase. The confirmation of this tP4 structure was done by measuring the d-spacing values of the reflecting planes parallel to zone axis $[0\ 1\ \bar{1}]$. The values of d-spacing corresponding to (1 1 1) and (2 0 0) planes are ~0.220 nm and ~0.190 nm respectively. The angle subtended by (1 1 1) and (2 0 0) is measured to be 56°.

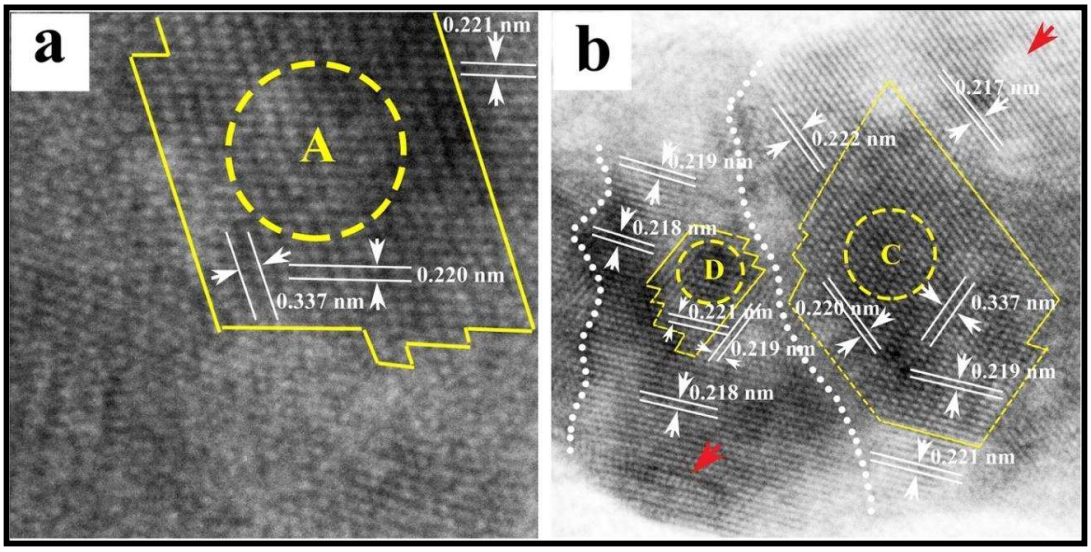

Figure 3.6: *High-resolution phase contrast image (higher magnification version of 3.5(a-b)) showing intermetallic phases grown within the solid solution phase of AuCu with sharp faceted interfaces.*

Figure 3.7d is the representation of (1 1 1) planes of cP4 (Au_3Cu) phase with inter-planar spacing of ~ 0.220 nm along [$\bar{1}$ 3 $\bar{2}$] zone axis. Figure 3.5c is shown in order to describe the nanotwin formation mechanism in Au/Cu multilayer thin film. In this high-resolution image, it has been observed that the lattice fringes appearing adjacent to either side of the amorphous Cu layer had d-spacing values ~0.220 nm and ~0.210 nm. The ~0.220 nm lattice spacing represents (1 1 1) plane of disordered cF4 (AuCu) phase whereas ~0.210 nm represents (1 2 0) plane of oP8 phase. The growth of nanotwin boundary at the Au/Cu interface among {1 2 0} planes of oP8 phases could also be seen with the twinning angle of ~106° marked with dotted line. The formation of twin boundary probably happened during coalescence of independently grown crystals [242,243].

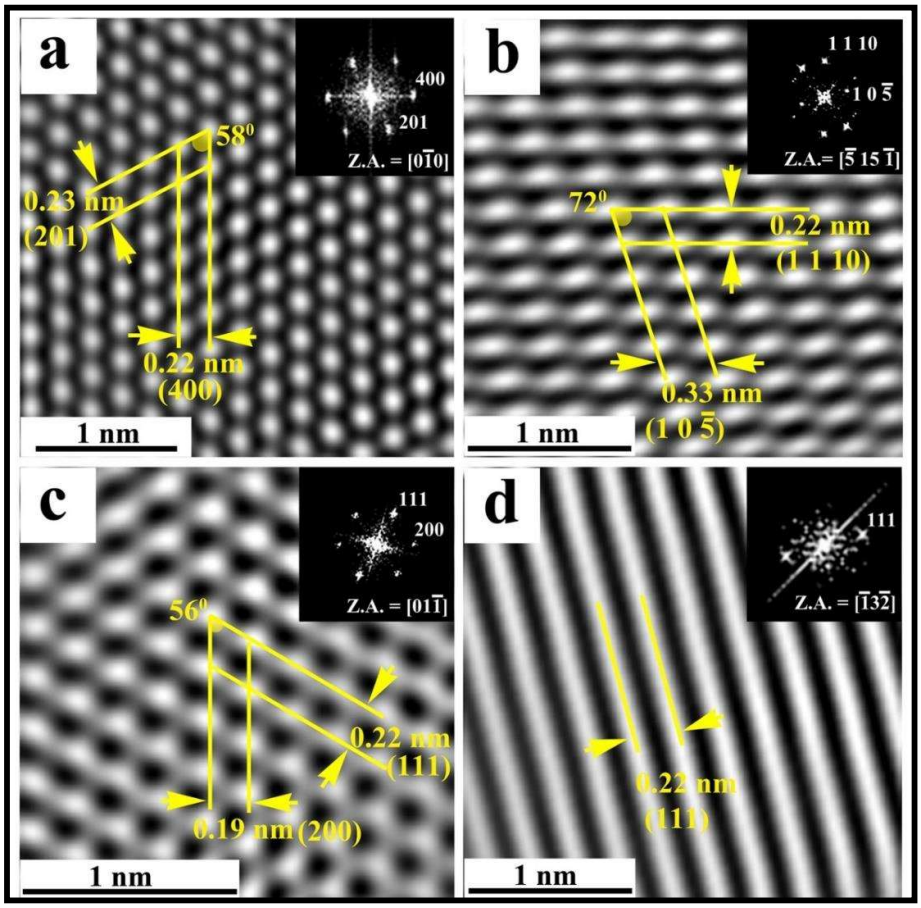

Figure 3. 7: *FFT-filtered high-resolution phase contrast images of ordered phases along with their corresponding FFTs (inset)* ***a)*** *AuCu (oP8) phase marked as 'B' in figure 3.5a* ***b)*** *AuCu (oI40) phase marked as 'C' in figure 3.5b* ***c)*** *AuCu (tP4) phase marked as 'D' in figure 3.5b and* ***d)*** *Au_3Cu (cP4) phase.*

It is clearly seen in this image (Figure 3.5c) that there are three domains specifically named as 'I', 'II' and 'III'. While coalescence, in order to reduce the interface energy, the twin boundary has formed between the domains 'I' and 'II'. This had happened in such a manner that when the coalescence of islands marked as 'I', 'II' and 'III' took place, the unfavorably oriented domain 'III' was consumed by the domains 'I' and 'II'. Since the energy of the nanoscale twin boundary is lower than the high angle grain boundary energy, the twin boundary formation is favored during the subsequent growth of Au/Cu interface and is found to be almost parallel to the growth direction of the film [244]. The rectangular facet

on the left side of the twin boundary is measured to be ~9 nm approximately whereas the other side facet is not clearly distinguished. The length (~ 9 nm) of the twin facets is closely related to the high deposition rate [245]. Twin boundary appeared up-to few nanometers clearly and beyond that it vanished. The region where this twin boundary has vanished is shown separately in figure 3.5e. Beyond the point up to which the twin boundary is visible, a moiré pattern with spacing ~0.49 nm has evolved. This moiré pattern is the indication that two or more crystals rotated or displaced with respect to one another are in juxtaposition [35]. In this particular case, it appears that {1 2 0} planes of two oP8 crystals have given birth to this moiré pattern due to relative rotation among them. This rotation has taken place so as to minimize the misfit strain generated during coalescence of more than two differently oriented islands. The coalescence of these islands occurs in order to minimize the elastic strain at each interface [4,146]. Such misfits are indicated by the arrows in figure 3.5e together with the disordered portion (encircled) generated owing to misfits and rotations.

In HRTEM images shown in figures 3.5(a-e), it has been observed that the size of the grains is smaller than the thickness of the film and most of the grain interiors are free of defects like dislocations etc. However, with varying defocus and tilting conditions, various misfit dislocations can be seen in bigger size crystals marked with arrows in figures 3.5b and 3.5c. This helps one to infer that the islands incorporating the dislocation are too large to rotate so as to minimize the misfit. However, one can see that the white contrasts (Figure 3.5c, encircled by white dotted ellipse) emerged out of strain associated with these misfits and were mostly found at the grain boundaries (homophase interface). Therefore, the grain boundaries shown in figure 3.5d looked like disordered white contrast region. This randomness occurred at the grain boundaries wherever more than two islands joined by

leaving a partial space amongst them. This was confirmed by measuring the d-spacing values of the surrounding grains. The d-spacings of these lattice fringes in surrounding grains showed little variation in them. The various factors that influence the values of d-spacing in surrounding grains of the same set of planes in HRTEM image include, deviation in the orientation of lattice fringes with respect to zone axis and signal strength originating from that particular lattice fringes containing background noise [139]. Some regions in HR images show sharp and clearly visible grain boundaries. The maximum width of this disordered region (Figure 3.5d) perpendicular to the grain interfaces was measured around ~ 1 nm. This randomness is equivalent to the four to five lattice plane spacing. The irregular curvature (dotted yellow curve) of this disordered boundary evolved due to the high and low misfit regions. Therefore, these low-energy and high-energy regions reflect continuous varying curvature in the disordered boundary. Based on the above observation it is understood that the mechanism of overall strain relaxation occurred at the junction created by coalescence of more than two islands in Au/Cu thin films.

When the ordered phases like tP4, oP8, oI40 were looked upon closely, the sharp interfaces could be seen at their peripheries. However, facets could be observed at their interfaces during their growth as shown in figures 3.5a and 3.5b. Such facets are formed due to the highly anisotropic surface energies associated with them [132,246]. In this order-disorder phase transformation, considerable structural changes have occurred. The disordered face centered cubic phase (cF4) is transforming to ordered primitive tetragonal phase (tP4) in one case whereas ordered primitive orthorhombic (oP8) and body centered orthorhombic (oI40) phases in other cases. In all such phase transformation processes, highly symmetric cubic phase is converting into less symmetric tetragonal and orthorhombic phases [142].

3.3.5 Multislice simulation and direct structure imaging

The mechanism behind the formation of phase contrast high-resolution images involves constructive and destructive interference among the direct and the diffracted electron beams resulting in the modulated emergence of fringes at the image plane. At the image plane the phase component of the interfered wave is lost and the amplitude part is retained on the image plane to form the image. Therefore, the obtained HR-image is not directly interpretable because it can be deceptive in appearance. These HR-images can be quantified and understood well only with the help of simulation technique.

The processed atomically resolved phase contrast image of oP8 (AuCu) with respect to [0 1 0] zone axis along with its corresponding FFT (inset) is shown in figure 3.7a. The planes (4 0 0) and (2 0 1) subtending an angle of 58° with their corresponding modulations of ~0.22 nm and ~0.23 nm are represented in the same image. However, there are two consecutive bright spots associated with a weak contrast in between. In order to identify the phase contrast in the oP8 phase, multislice simulation has been carried out. The simulated defocus –thickness map for oP8 phase along Z = [0 1 0] zone axis is represented in figure 3.8a. A variation in contrast can be seen in the simulated image depending on the thickness and defocus values. When the simulated image in the thickness range ~10-12 nm and defocus ~104-105 nm is compared with the experimental image, it matches well with the experimental image as shown in figure 3.7a. When the crystal is projected along [0 1 0] direction and it is overlaid on the simulated map, it is observed to be an alternate horizontal stacking of Au and Cu (outset of the simulated defocus-thickness map). However, all the vertical columns (outset of the simulated map), which are essentially mixed in chemistry with Au and Cu are not imaged simultaneously. Only the alternate vertical columns out of

a band of three are imaged, and both sides of the band, which are free of any such atom column produces a spurious atom column like contrast.

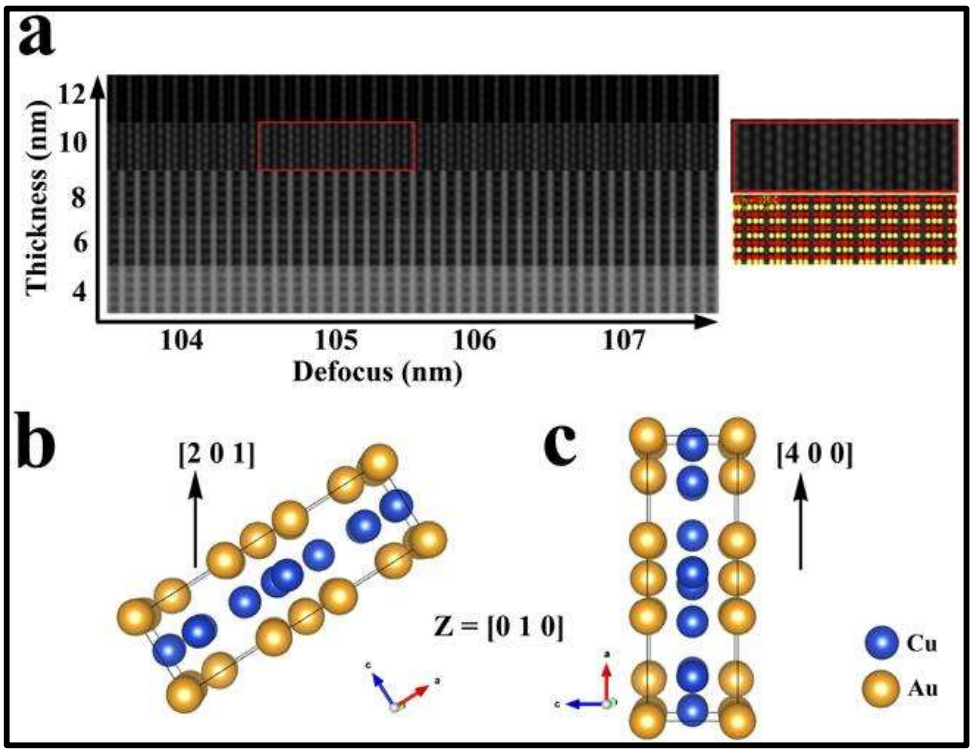

Figure 3.8: a) *Defocus-thickness map for the AuCu (oP8) phase generated by multislice simulation method along Z = [0 1 0] zone axis. The parameters used in simulation are voltage = 200kV, C_S =1.2 mm and Δf_{Sch} = −65.83 nm. The close match of simulated image with the experimental image for AuCu (oP8) phase is found at t ~ 10 nm and Δf ~ 105 nm. In the simulation red colour represents Cu and yellow colour represents Au.* ***b)*** *Perspective view of unit cell of AuCu (oP8) phase projected along Z = [0 1 0] direction with upward vector [2 0 1],* ***c)*** *same unit cell projected along Z = [0 1 0] with upward vector [4 0 0].*

Moreover, the variation in contrast is also seen within the bright layer generated due to absence of atomic columns. The unit cell of the oP8 phase projected along [0 1 0] direction with two different upward vectors e. g. [2 0 1] and [4 0 0] are shown in figures 3.8b and 3.8c respectively. From both the projection diagrams alternate stacking of Au and Cu could easily be discerned. However, closer look at the projected structures, simulated high

resolution image and the experimental image in figure 3.7a indicates that under the given experimental condition bright contrast does not represent atom columns. It is essentially the inter-columnar space that is imaged and the faint delocalized contrast in between two bright contrast regions represents some of the atom columns of the structure. It will require exit phase wave reconstruction in order to understand as to why such contrast pattern develops and it is currently out of scope for this study. From this image, direct mapping of the Au and Cu atom columns or the presence of atomic scale defects is not possible to be inferred in this structure.

High-resolution phase contrast image of oI40 phase along Z= $[\bar{5}, 15\ \bar{1}]$ zone axis along with its corresponding FFT (inset) are shown in figure 3.7b. The angle subtended by $(1\ 0\ \bar{5})$ and (1 1, 10) planes is 72° as represented in the figure 3.7b. Lattice fringe spacings corresponding to $(1\ 0\ \bar{5})$ and (1 1, 10) planes are measured to be ~0.220 nm and ~0.330 nm respectively. A strong and weak modulated bright contrast could be observed along both (1 1, 10) and $(1\ 0\ \bar{5})$ planes. In order to understand the origin of this contrast, a defocus-thickness map generated by multislice simulation under 200 kV operating voltage and C_s = 1.2 mm is given in figure 3.9a. A simulated image in the thickness range ~22-28 nm and defocus ~149-150 nm exhibits a close match with the experimental image. However, careful investigation of the simulated image indicates that the diffuse white contrast developed in between the two consecutive strong white spots in simulated image is not clearly resolved in the experimental image. There could be several factors, which might lead to such kind of appearance and it has been discussed in earlier literature [247]. These weak spots only appeared along the (1 1, 10) layers and not along $(1\ 0\ \bar{5})$ layers. When the projected structure of oI40 phase along Z = $[\bar{5},\ 15\ \bar{1}]$ is overlaid onto the simulated image, it is clearly observed that the bright spotty contrast arises from the inter-columnar space.

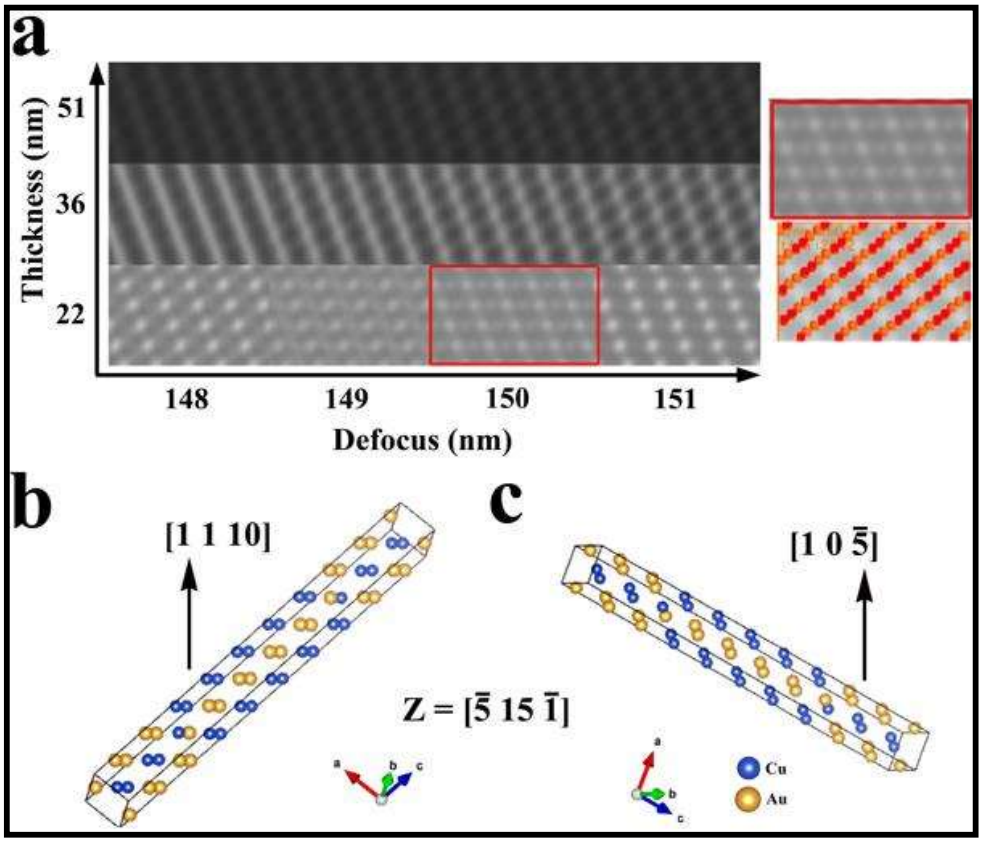

Figure 3.9: a) *Defocus-thickness map for the AuCu (oI40) phase generated by multislice simulation method along Z =* $[\bar{5},\ 15\ \bar{1}]$ *zone axis. The parameters used in simulation are voltage = 200kV,* C_S *=1.2 mm and* $\Delta f_{Sch} = -65.83$ *nm. The close match of simulated image with the experimental image for AuCu (oI40) phase is found at t ~ 22 nm and Δf ~ 150 nm.* ***b)*** *Perspective view of unit cell of AuCu (oI40) phase projected along Z =* $[\bar{5},\ 15\ \bar{1}]$ *direction with upward vector [1 1, 10]* ***c)*** *same unit cell projected along Z =* $[\bar{5}, 15\ \bar{1}]$ *with upward vector* $[1\ 0\ \bar{5}]$.

The weak contrast in between two bright spotty contrast represents some of the atom columns. The perspective view of oI40 structure projected along $[\bar{5}, 15\ \bar{1}]$ direction with upward vector [1 1, 10] and $[1\ 0\ \bar{5}]$ is represented in figures 3.9b and 3.9c respectively. A combined set of two Au or Cu atoms arranged in alternate sequence could be observed in both the projections. This kind of arrangement of Au and Cu atomic columns results in an elongated bright spot contrast in an experimental image of oI40 as shown in figure 3.7b.

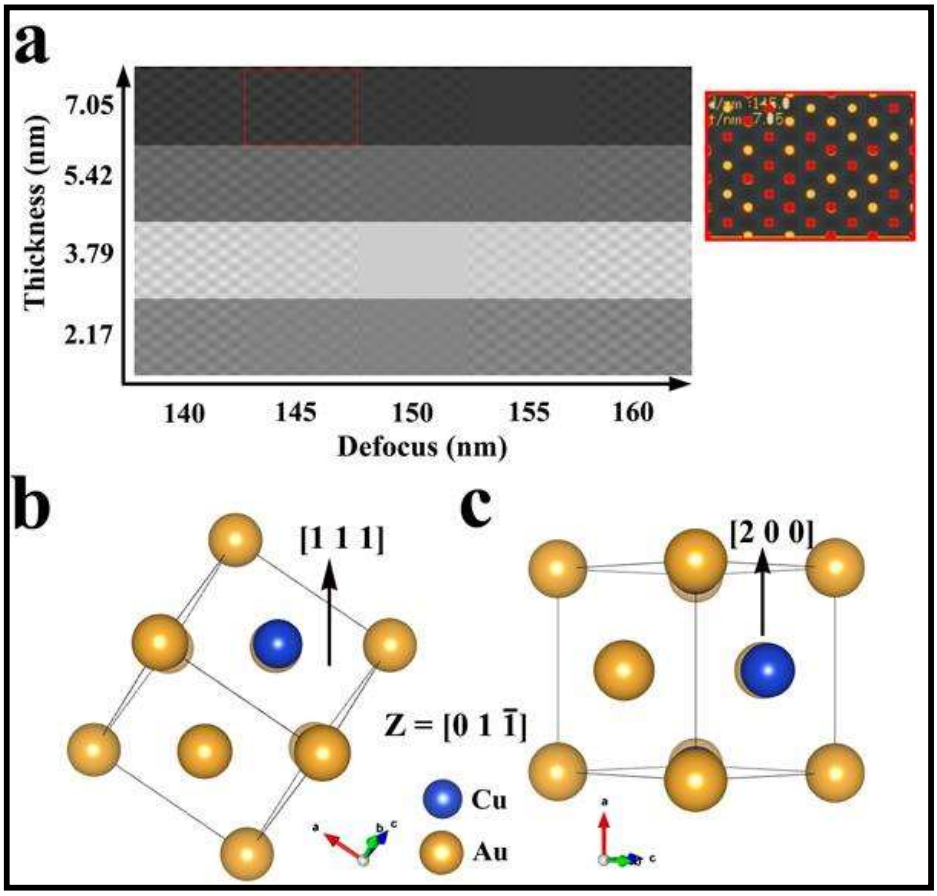

Figure 3.10: a) *Defocus-thickness map for the AuCu (tP4) phase generated by multislice simulation method along Z =* [0 1 $\bar{1}$] *zone axis. The parameters used in simulation are voltage = 200kV,* C_S *=1.2 mm and* $\Delta f_{Sch} = -65.83$ *nm. The close match of simulated image with the experimental image for AuCu (tP4) phase was found at t ~ 5-7 nm and Δf ~ 140-145 nm.* ***b)*** *Perspective view of unit cell of AuCu (tP4) phase projected along Z =* [0 1 $\bar{1}$] *direction with upward vector [1 1 1]* ***c)*** *Same unit cell projected along Z =* [0 1 $\bar{1}$] *with upward vector [2 0 0]. The contrast arising out as bright spots represents Au and Cu atomic columns.*

The phase contrast high-resolution image of the tP4 structure along [0 1 $\bar{1}$] zone axis with its corresponding FFT (inset) is shown in figure 3.7c. The lattice spacings corresponding to (1 1 1) and (2 0 0) planes are ~0.220 nm and ~0.190 nm respectively. The angle measured between these two planes is 56°. A regular symmetry of bright spots can be observed in

figure 3.7c. In order to understand this contrast, a defocus –thickness map for tP4 phase along [0 1 $\bar{1}$] direction is generated by multislice simulation approach and is shown in figure 3.10a. Simulated image in the defocus range of ~140-145 nm and in the thickness range ~6-8 nm is found to be matched with experimental image. When two-dimensional structure of tP4 phase is projected along [0 1 $\bar{1}$] direction and it is compared with the simulated image, it becomes clear that the bright spots are the result of potential arising out from the alternating Au and Cu atom columns. A three-dimensional unit cell of tP4 structure projected along [0 1 $\bar{1}$] direction with [1 1 1] and [2 0 0] vectors representing upward directions have been shown in figures 3.10b and 3.10c respectively. The projection depicts alternating Au and Cu atom columns arranged in a periodic fashion. Therefore, the potential from each of these atomic columns had been reflected as a bright spot in the processed experimental image of tP4 as represented in figure 3.7c.

Atomically resolved phase contrast image of ordered Au_3Cu (cP4) phase in processed condition is shown in figure 3.7d. A bright and dark alternate layered contrast could be observed all-throughout this experimental image. The spacing between these two consecutive bright layers is measured to be ~0.227 nm. This spacing later on matched with the {1 1 1} planes of cP4 phase. In order to understand this layered bright and dark contrast, this ordered cP4 phase was simulated along [$\bar{1}$ 3 $\bar{2}$] zone axis using multislice method. This zone axis was chosen because this was the closest zone possible in cubic structure through which {1 1 1} planes could be seen. Therefore, the simulated diffraction pattern along [$\bar{1}$ 3 $\bar{2}$] zone was generated and displayed in figure 3.11c, so as to clear the overall picture of the diffracting planes. The simulated defocus-thickness map has been generated for cP4 phase, which is shown in figure 3.11a. This map was generated by keeping the microscopic conditions such as spherical aberration C_s = 1.2 mm and operating voltage at 200kV.

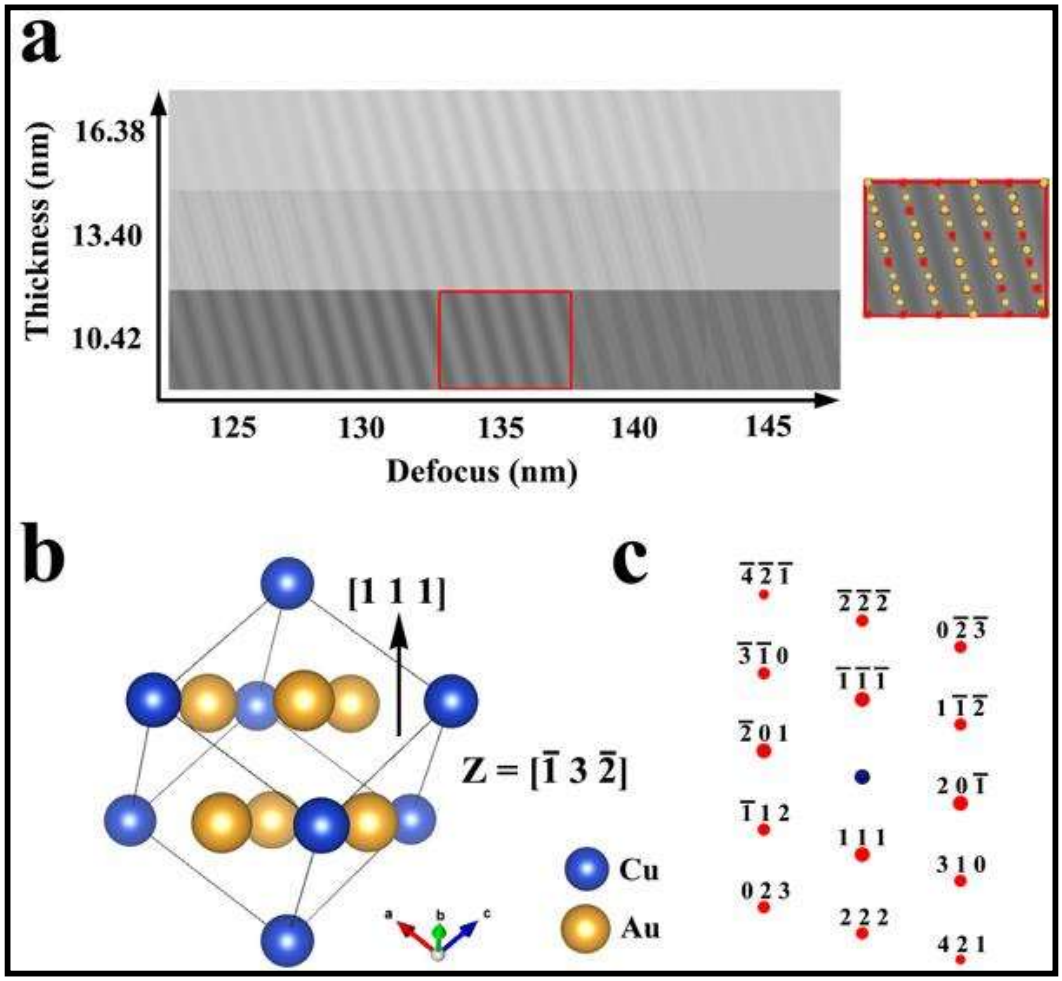

Figure 3.11: a) *Defocus-thickness map for the AuCu (cP4) phase generated by multislice simulation method along Z =* $[\bar{1}\ 3\ \bar{2}]$ *zone axis. The parameters used in simulation are voltage = 200kV,* C_S *=1.2 mm and* $\Delta f_{Sch} = -65.83$ *nm. The close match of simulated image with the experimental image for AuCu (cP4) phase is found at t ~ 10-12 nm and Δf ~ 130-135 nm.* ***b)*** *Perspective view of unit cell of AuCu (cP4) phase projected along Z =* $[\bar{1}\ 3\ \bar{2}]$ *direction with upward vector [1 1 1]* ***c)*** *Simulated diffraction pattern of AuCu (cP4) phase along* $[\bar{1}\ 3\ \bar{2}]$ *zone.*

When the experimental image of cP4 is compared with the simulated map, the closest match is found in the defocus range ~130- 135 nm and in the thickness range ~8 -11 nm. When the three dimensional atomic structure of cP4 in real space is projected along $[\bar{1}\ 3\ \bar{2}]$ direction, it becomes clear that the bright contrast is comprised of Au and Cu atom columns

whereas dark contrast represented the absence of atomic columns. The arrangement of Au and Cu atoms within a single unit cell of cP4 structure projected along $[\bar{1}\ 3\ \bar{2}]$ direction with a [1 1 1] vector pointing upward direction has been represented in figure 3.11b. The sites occupied by Au and Cu atoms within the (1 1 1) plane could be viewed clearly in a direction perpendicular to [1 1 1] vector. Consequently, the contrast emerged out as a bright layers reflects the presence of Au and Cu atoms arranged in a manner as shown in figure 3.11b.

3.4 Discussion

Deposition of Au/Cu multilayer thin films onto polycrystalline Si substrate, determination of phases in the multilayer through GIXRD, experimental observation of the multilayer interface by HRTEM coupled with simulation, generates exciting information about phase evolution, growth morphology and kinetics of thin film growth in Au/Cu system. Several phases, which are non-existent in the equilibrium phase diagram appear in the thin film, as metastable phases. It appears that there is a wide metastability landscape in the Au-Cu alloy system, where the system may get locked in a local energy minimum. Detailed understanding of this, in addition to enhancement of fundamental understanding, may contribute in formulating new robust strategies for application of this alloy in nanotechnology and related fields. Additionally, nuances of imaging the interfaces and understanding complicated structures by direct electron structure imaging will be discussed in the subsequent sections.

3.4.1 Phase evolution, growth morphology and kinetics

The GIXRD pattern of the 40TAu multilayer thin film clearly shows peak broadening and occasional peak splitting. Based on the peak broadening and splitting, it can naturally be inferred that the grain size in the multilayer is small and local strain is present in the film,

which is further confirmed by TEM studies. In nanostructure literature, peak broadening and splitting with minor shift are attributed to small grain size and presence of local strain [104]. This should be the case if one is dealing with a single-phase material. However, in the present case extensive simulation of X-ray diffraction pattern of several ordered phases in Au-Cu system and its careful comparison with the experimental pattern reveals that all those phases, even though in minor quantities, are present in the multilayer. It has been further substantiated by electron diffraction. Recently, Mourya et al. [125] in their structural investigation of copper indium sulphide/selenide (CIS) crystal in the pure and doped form have reported similar broadening and shift in peaks and they have proved that the broadening is due to the nanoscale composition separation in the crystals that may profusely change the functional properties [192]. It is important to study the experimental results beyond conventionally accepted protocols and that may open up new insights about nanoscale functionalities owing to metastable phase transformations at nanoscale. A number of structural transformations reported recently in Au-Cu alloys at such length scales are relevant in this regard [65,110,248].Thin film growth at room temperature strongly depends on the chemisorption of the incoming species, formation of its cluster and final coalescence of those clusters [133,135]. Surface enhanced diffusivity is one of the rate controlling factors and that is why it is often observed that the growth rate is dependent on the melting point of the thin film material [49,249]. In the present study, the melting point of Au (~1064 ^{o}C) and Cu (~1085 ^{o}C) are quite close to one another and it is not expected to make a huge difference in growth behavior. However, during thin film growth it was planned to grow each layer ~40 nm thick. Cross-sectional TEM (XTEM) observation indicates that the individual film thickness is less than the intended thickness and the interface is wavy. During thin film growth, the thickness was monitored by a quartz crystal

balance. The crystal balance is supposed to monitor the vibrations created by the impact of the atoms during deposition. The fact is that external vibrations interfere with those created during deposition process. The vibrations created due to atom deposition is the only parameter that is supposed to be measured by the quartz crystal balance. Owing to the interference, actual deposition thickness as measured by the crystal balance may produce erroneous results. Another factor that might have contributed to it is the applied vacuum, which was ~4 x 10^{-6} Torr in the present case. The accuracy in thickness measurement gets better with high value (> ~10^{-7} Torr) of vacuum [4,49]. The presence of these undulations at the interfaces of Au/Cu may be attributed to many factors. They include 1) inter-diffusion of Au and Cu atoms into one another across the interface, 2) Mismatch between lattice parameters of Au and Cu resulting in generation of strain and its non-uniform distribution, 3) local variation in the kinetic energy of the Au and Cu atoms while impingement, 4) difference in the size of island formation and its subsequent coalescence, 5) migration of surface atoms while deposition leading to the formation of facets, steps and/or defects in order to reduce local surface energy [39,156,246]. As vapor deposition process is relatively less energy intensive process [44], concentration of Au and Cu is less distributed and individual nuclei grow on the top of the pre-existing film. One expects the ideal smooth and flat surface when the deposited thin film possesses minimum surface energy and the number of crystallographic variants with minimal surface energy at the interface is not too many[133]. The undulated morphology in the present study definitely indicates that the surface energy might not be at its minimum and there may be many crystallographic variants available at the interface. However, the interface formation is a statistical process. It basically governs the smoothness of the surface, which includes the adatom surface mobility, nucleation and growth. The average surface roughness of the multilayer Au/Cu

thin film has been calculated to be ~7.7 nm utilizing previously reported correlation between the roughness and film thickness based on the Poisson distribution [152].

From the XTEM images, the columnar morphology in the Au layer is clearly discerned. It is understood from the micrograph that the columnar growth is basically due to the limited adatom mobility, geometrical constraints and shadowing effects of the neighboring growth islands. The deposition process started with the formation of nuclei onto the surface of the Cu layer first, subsequent coalescence and geometrical shadowing effects lead to the columnar growth. The morphology of the Au/Cu thin films, which was thermally evaporated under high vacuum conditions exhibited less dense packing efficiency of columns and adapted a convex curvature towards the direction of the columnar growth. Based on the applications, these columnar growth morphologies in the Au/Cu thin films can be treated as beneficial in some cases whereas undesirable in the other. Ultimately, the columnar growth depends on the evolution of islands followed by its growth. This evolution of islands in the Au layer deposited on Cu layer manifested the wetting behavior of the Au nuclei on Cu layer [44]. Cross-sectional microscopy observation indicates that the columns are often perpendicular to the interface with a very few exceptions of inclined columns. The inter-columnar space is also not tightly packed. Based on this observation, it had been understood that the width and length of the individual columns increased with the Au layer thickness. Consequently, a proportional relationship is identified amongst the diameter and thickness of columns present in Au layers. The overall surface morphology of the Au/Cu multilayer thin films has been found to be governed by the thickness of Au layer. The diffraction pattern from the multilayer consists of a large number of spots against the background of a diffused halo. It has been shown in preceding section that the spots arise out of several ordered phases that form at the interfaces of Au/Cu multilayer. However, the

Cu layer is largely amorphous. The time available for the crystallization of Cu was not enough, which resulted in a kinetic bypassing of the otherwise thermodynamically spontaneous process. Slow kinetics exhibited by Cu atoms in the present study is attributed to the following reasons: 1) The deposition rate of the Cu monolayer is faster than the jump frequency of the adatoms of Cu to its equilibrium ordered position by surface diffusion 2) The stability of amorphous Cu layer is due to the formation of Cu atom clusters of different sizes (< 1 nm) locking each other in place and restricting the long range diffusion of atoms, which promotes crystallization and, 3) based on the information available in literature, mobility of atoms decreases with the increasing (but not always) melting point of metals [49]. Even though the melting points of Au and Cu are very close to one another, it is the ratio of the deposition temperature to the melting point that defines the efficacy of the diffusion process [4]. The schematic view of the cross section of the multilayer is given in the figure 3.12. In the figure 3.12, the morphology and the structure of the phases as obtained from the electron microscope observation are given along with their dimension.

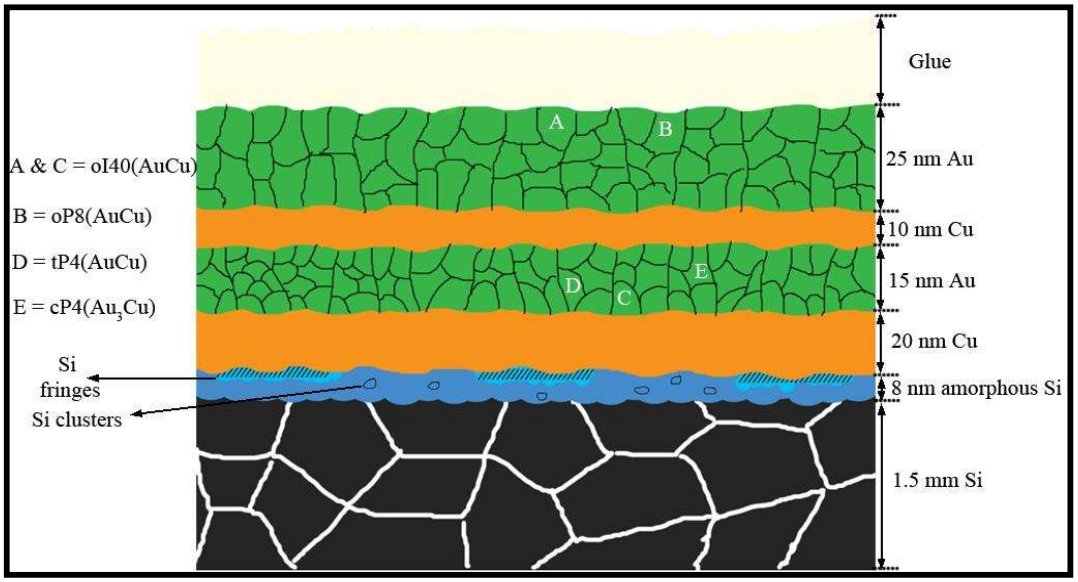

Figure 3.12: *Schematic representation of the microstructure and interface of the Au/Cu multilayered thin film cross-section.*

3.4.2 Amorphization at the interfaces and associated challenges

From the electron microscopy investigation, it has been observed that the Au layer is crystalline while the Cu layer is amorphous. This observation is attributed to the slower crystallization kinetics of Cu. Initially, the Si substrate was polycrystalline. However, after deposition of Cu layer, a thin amorphous layer has been formed. This amorphous layer extends to varied depths into the Si substrate before lattice fringes corresponding to Si could be observed. The amorphous layer might have formed inside the Si substrate due to the kinetic impingement of Cu atoms onto the Si substrate (Figure 3.12). The irregularity in the depth of this reaction suggests that wherever the Cu impingement was with higher kinetic energy, there the penetration of Cu was more inside the substrate. This observation led us to understand that the defect cascade forms very locally and it starts with the introduction of strain fields and defects in the lattice. Extensive defect cascade formation may lead to amorphization [239].

This defect cascade might have partially formed during kinetic impingement of Cu atoms onto the Si substrate during deposition. There is a possibility of such defect cascade formation during ion-milling. However, as the ion-milling was done with a very low voltage, viz., 3kV at a low angle of incidence of 3-4°, the possibility of extensive defect cascade formation during ion-milling is not very likely [250]. In addition, while obtaining the HR lattice-fringe images, there is also a possibility of thermal mixing of atomic species due to the interaction with high-energy electron beam. The different contrast arising at the interface region may be a combined effect of extensive reaction of adatoms with substrate and thermally induced defect cascade. High resolution imaging of thin film interfaces has remained to be a formidable challenge as nature of interface may change during ion-milling and electron imaging. During high-resolution imaging, the condenser lens current was kept

at a very low value. Moreover, extensive ion milling or electron beam damage would have manifested itself as amorphization deep inside the Si substrate, which has not happened in the present case. In this light, it is imperative to assume that while Cu is deposited onto polycrystalline substrate it produces a very thin and discontinuous amorphous layer at the interface.

3.4.3 Structure evolution of multilayer and interfaces

The growth morphology of the multilayer thin film, its thickness and the reactive nature of the interfaces have been discussed in the earlier sections in the light of growth kinetics and the influence of processing parameters while thin film deposition. Localized amorphization of the Cu-Si interface also has been discussed as a consequence of defect cascade formation due to the bombardment of Cu atoms during deposition. However, the possibility of partial local amorphization during ion beam thinning of the cross section sample cannot be ruled out. Low ion beam current, small value of the angle of incidence and above all limited time exposure of the interface to the ion beam has been argued to be the less important factors. It cannot therefore be placed on record beyond ambiguity that defect cascade formation due to Cu atom impingement is the sole responsible factor behind local amorphization. When the Au layer is deposited onto the Cu layer, it has been observed that it is never pure Au, instead it is almost always either a solid solution of Au and Cu or an intermetallic phase of Au and Cu. Some of the intermetallic phases are not even present in the phase diagram. This observation proves that local diffusion couples are formed while deposition of Au on Cu or vice-versa. It might be argued that the diffusion induced products formed during ion beam thinning, which has been reported in earlier literature [144,237,251]. It is worth-noting that in the present work the ion beam milling was done at cryo-temperature. At such a low temperature diffusion induced new phase formation is ruled out. In the present case,

the similar phases have been observed in GIXRD results, which has been further verified by simulation. The GIXRD sample is never exposed to the ion beam. So it can be concluded undoubtedly that the local diffusion couples form while growing the thin films multilayers. The evolution of various phases in diffusion couples has been a formidable problem and it becomes complicated when it is a nanostructured multilayer [252] . Corroboration of GIXRD and TEM data leads to the understanding that in most of the multilayers the crystalline phase is cF4 solid solution phase of Au and Cu. The solid solution phase is a stable phase as predicted by the phase diagram (Figure 3.1). However, in some localized regions, the tP4 (AuCu) phase can also be observed. In addition to that local precipitation of oP8 (AuCu) and oI40 (AuCu) phases can also be observed. Although, it might appear that the tetragonal and orthorhombic phases are quite different from the solid solution phase, a distinct thread of connection can be established between them.

The solid solution phase is likely to experience local composition fluctuation while the deposition is carried out. A number of solid solution phases of Au and Cu with varying composition has been reported in literature [112,113,222,253]. The lattice parameter of 50-50 atomic% solid solution of Au and Cu is ~0.385 nm and that of 88-12 atomic% solid solution of Au-Cu is ~0.403 nm. While the lattice parameter of tetragonal AuCu are a = 0.396 nm and c = 0.367 nm. It can be clearly seen that expansion along the ‘a’ and ‘b’ axes and contraction along the ‘c’ axis accompanied with ordering may lead to this structural transformation. So, the tetragonal AuCu phase may be seen as a structurally ordered phase, which has been polymorphically transformed from the solid solution of Au and Cu. The observed local composition variation may be seen as the responsible factor behind this structural transformation. However, the associated and underlying local electronic structure

changes also needs to be looked at carefully for understanding the change in electronic behavior, especially in evaluating the functional properties of such thin films.

Another phase that has been observed locally, mainly at the Au/Cu interface is the oI40 phase. This phase is quite complicated in structure and it is often termed as the chimney-ladder structure. This phase belongs to the category of classical long period superstructures. This phase is not unambiguously reported as an equilibrium phase in the phase diagram. Appearance of such a phase at the interface of Au/Cu nanostructured multilayer does not apparently bear any correlation with the solid solution phase. The [1 0 0] type orthographic projection of this phase is given in figure 3.13.

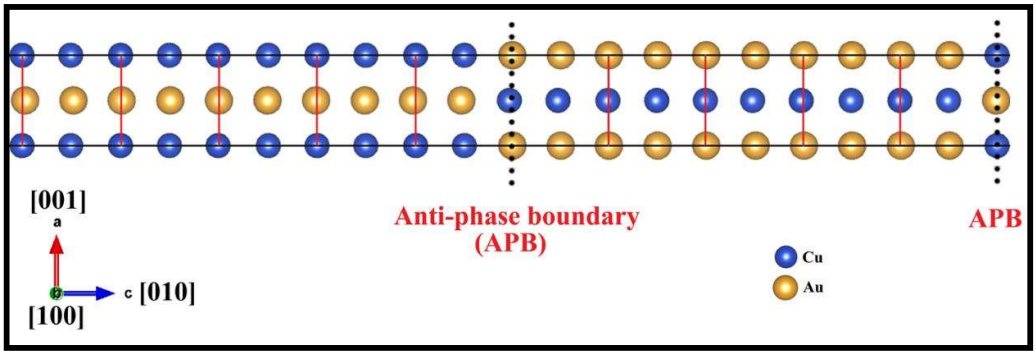

Figure 3.13: *Schematic representation of the AuCu (oI40) supercell consisting of ten AuCu (tP4) unit cells. Presence of anti-phase boundary with <½ ½ 0> translation vector after every five unit cells is indicated by the dotted black line.*

It is observed from the figure 3.13 that the ordered tetragonal AuCu phase is stacked along [0 1 0] direction and after every five cell an anti-phase boundary (APB) with ½ [1 0 $\bar{1}$] translation vector is introduced then the repeating length of the crystal gives birth to oI40 structure with a specific APB density i.e., 0.1/unit cell. At this juncture the oI40 structure can be seen as a derivative of the tP4 structure with periodic introduction of APBs whereas, the tP4 structure represents a degenerate state of the oI40 structure. As mentioned earlier, tP4 is a polymorphic derivative of the cubic solid solution phase and this establishes a clear

link between the solid solution phase and the oI40 phase. It may be important to ask a question at this point, as to why the APBs are not visible under the TEM. It is worth-mentioning here that APBs with such specific translation vectors will give birth to δ-fringe contrast in diffraction contrast imaging under the two-beam excitation of very specific diffraction vectors. Which is often not possible and in the present case it has not been done. Secondly, it has been shown by direct structure imaging that phase contrast images most often represent cluster of atoms (Section 3.3.5). So, APBs are not clearly seen. Such kind of long period superstructures have been reported for DO_{22} (Al_3Ti), DO_{23} (Al_3Zr) etc. [254,255]. It is important to recall based on observations in literature that two dimensional magnetic artificial superstructures based on FePt etc., is also off-spring of the same concept [256]. However, all of them have very different properties. It is believed that formation of oI40 phase might be quite low in volume fraction, however, its effect on functional properties may be significant [100,228]. In a similar line, the oP8 phase may also be seen as a derivative of the solid solution phase where specific directional ordering plays an important role.

It is worth-reiterating at this point that the GIXRD pattern of the multilayer appeared to be solid solution of Au and Cu. Careful analysis and simulation, hinted at the possibility of the presence of several other ordered phases, which are apparently very different in structure. Their presence has been confirmed through electron microscopy. In the preceding section, the underlying connection between the phases have been established. It is bound to affect the functional properties of the multilayer. Several exciting properties of nanostructured Au and Au-Cu solid solutions have been reported in literature [100,223,228] Almost always, the origin of the exciting properties has been attributed to the high surface to volume ratio. In addition to this, local structural changes may occur leading to such

changes, which has remained almost unexplored till date barring a few exceptions. The nature of the interfaces between the cubic solid solution phase and the intermetallic phases, and the type of transformation that leads to the precipitation of the ordered phases in the solid solution matrix has remained to be an intriguing question [257,258]. In the present study a definite clue about the nature of the interface has been obtained. In reference to the figures 3.5 and 3.6, it has been observed that the facet with ~0.220 nm spacing of oI40 phase is parallel to the ~0.221 nm spacing of cF4 (AuCu) solid solution phase. The relative strain introduced by such alignment is ~ 0.4%. This strain is assumed to be across $(1\ 0\ \bar{5})$ facet of oI40 phase. Similarly, as seen from the figure 6b, ~0.221 nm plane of tP4 (AuCu) is aligned with the ~0.218 nm plane of cF4 structure. In this case the relative strain across the 111 interface is ~1.3%. Consequently, the interface boundary is likely to be semi-coherent. It has been pointed out in earlier literature that free energy change associated with the precipitation of such ordered phases within the cubic matrix evolves from the bulk free energy of the new phase, interface energy, and energy associated with any defect in the structure or in the interface [136].

It has been pointed out earlier that defect energy is vanishingly small in the long period superstructures. The interface energy is also likely to be small because of the semi-coherent nature of the interface and small value of strain associated with it. So, the energy cost for such a transformation is likely to be low, which often permits the system to hop from one minima to another, within small volumes. The nature of such transformation in this system, whether homogeneous or heterogeneous, has been debated since long [229]. The present high-resolution observation (Figure 3.5 and 3.6) indicates that the mode of transformation is homogeneous in which atomically flat transformation facets move into the matrix. Extensive simulation of the high-resolution images of the ordered structures indicates that

most of the time cluster of atoms is imaged instead of individual atoms (Section 3.3.5). As a result of which atomically delineating the interface structure remains a challenging task. However, as indicated by Howe and co-workers, the interface is diffused in nature [115]. It is difficult to see and distinguish an atomically flat plane across which the structure changes abruptly. As structure imaging indicates, in the high-resolution image, a cluster of atom columns is imaged together instead of a single atom column and this eludes further quantification of the diffuse interface.

3.4.4 Metastability landscape of the Au-Cu phase diagram

Equilibrium phase diagram of Au-Cu has remained to be an enigma for several decades [104]. Sustained research efforts have led to the answers pertaining to some fundamental problems [115,229]. Complications associated with nanoscale and high surface to volume ratio have made several issues ambiguous to a large extent. The equilibrium phase diagram of Au-Cu is given in figure 3.1. It is observed from the phase diagram that at temperature above 400 °C, the cubic solid solution phase of Au and Cu is the stable phase. However, at lower temperatures, several phases start appearing, as some of them have been observed in the present case also. At the lower temperatures in the Au-Cu phase diagram, the phase boundaries are dotted, which necessarily means that the stability regimes between the phases cannot be distinguished so easily. Across the phase boundaries apart from the solid solution phase, tetragonal AuCu, orthorhombic AuCu II and order-disorder transformation related Au_3Cu or Cu_3Au phases can be observed. It has been established in the earlier section that even though the tetragonal and the orthorhombic phases appear to be quite uncorrelated with the cubic solid solution phase, both phases may be seen as derivative of the cubic phase. As the energy required for the cubic to tetragonal transformation is very

small, the system might hop from one state to another on introduction of little fluctuation of energy input from outside the system [136].

In a similar way, it can be argued that in the event of APB energy being vanishingly small, the tetragonal phase may transform into the orthorhombic phase very easily. In fact, the vanishingly small values of APB energy for long period superstructure phases has been reported in earlier literature [113,232,259,260]. It can be postulated from the current results and the published literature that the energy landscape for the Au-Cu system is shallow and there do exist several energy minima with very little or almost no difference in energy, so that the system may jump from one state to the other with relative ease. This is the most probable reason as to why phase boundaries have remained dotted even after several decades of sustained effort [261]. With the advent of nanotechnology and with the introduction of complicated processing conditions, multiple phase formation has become even more probable as most often the processing conditions are not quasi-static, making it more probable for a system to jump from one energy minima to another [262]. However, Au-Cu alloy system is beginning to be realized as one of the most potent systems for several applications ranging from catalysis, electronics, nanotechnology, packaging to biology and targeted drug delivery. In order to understand the novel functionalities of these systems, atomic scale understanding of structure and interfaces are quite important. In addition, first-principle calculation of energy of these phases and the interfaces will definitely go a long way in quantitative understanding of stability and functionality. However, this has not been attempted here.

3.5 Conclusions

The following conclusions can be drawn from this part of investigation:

1. The Cu layer is amorphous and the Au layer primarily consists of disordered solid solution phase of Au and Cu in the multilayer thin film of Au/Cu deposited on polycrystalline Si substrate. Additionally, tP4 (AuCu), oI40 (AuCu), oP8 (AuCu) and cP4 (Au_3Cu) phases are also observed in minor quantities in the Au layer and at the interface of Au and Cu layers.
2. The ordered intermetallic phases are polymorphically related to the disordered solid solution phase of Au and Cu. The ordered intermetallic phases grow into the solid solution phase by homogeneous transformation. The interfaces between the ordered intermetallic phases and the solid solution phase are semi-coherent with very little strain.
3. Energy requirement for the transformation of solid solution phase to ordered intermetallic phases in multilayer Au/Cu thin films being minimal, the system can locally nucleate such phases, which might play a very important role in determining their structural and functional properties.
4. Structural similarity and energy equity between the solid solution phase and the ordered intermetallic phases makes it difficult to determine their stability regime in the temperature composition space and that partially explains the existence of dotted phase boundaries in Au-Cu phase diagram. In the nanoscale regime, the problem is even more complicated because of the abruptly changed surface to volume ratio.